J. Fluid Mech. (2006), *vol.* 546, *pp.* 123–152. © 2005 Cambridge University Press
doi:10.1017/S0022112005007093 Printed in the United Kingdom

A noise-controlled free shear flow

By MINGJUN WEI AND JONATHAN B. FREUND

Department of Theoretical and Applied Mechanics, University of Illinois at Urbana-Champaign, Urbana, IL 61801, USA

(Received 2 January 2005 and in revised form 28 June 2005)

The adjoint of the perturbed and linearized compressible viscous flow equations is formulated in such a way that its solution can be used to optimize control actuation in order to reduce flow-generated sound. We apply it to a direct numerical simulation of a randomly excited two-dimensional mixing layer, with inflow vorticity-thickness Reynolds number 500 and free-stream Mach numbers 0.9 and 0.2. The control actuation is implemented as general source terms in the flow equations (body forces, mass sources, and internal energy sources) with compact support near the inflow boundary. The noise to be reduced is defined by a space–time integral of the mean-square pressure fluctuations on a line parallel to the mixing layer in the acoustic field of the low-speed stream. Both the adjoint and flow equations are solved numerically and without modelling approximations. The objective is to study the mechanics of the noise generation and its control. All controls reduce targeted noise with very little required input power, with the most effective (the internal energy control) reducing the noise intensity by 11 dB. Numerical tests confirm that the control is not by any simple acoustic cancellation mechanism but instead results from a genuine change of the flow as a source of sound. The comparison of otherwise identical flows with and without control applied shows little change of the flow's gross features: the evolution and pairings of the energetic structures, turbulence kinetic energy, spreading rate, and so on are superficially unchanged. However, decomposition of the flow into empirical eigenfunctions, as surrogates for Fourier modes in the non-periodic streamwise direction, shows that the turbulence structures advect downstream more uniformly. This change appears to be the key to reducing their acoustic efficiency, a perspective that is clarified by comparing the randomly excited mixing layer to a harmonically excited mixing layer, which is relatively quiet because it is highly ordered. Unfortunately, from the perspective of any practical implementation with actuators, the optimized control identified has a complex spatial and temporal structure, but it can be simplified. Two empirical eigenmodes were required to represent it sufficiently to reduce the targeted noise intensity by about 50 %. Optimization of a simple single-degree-of-freedom control with an *ad hoc* spatial structure is less effective.

1. Introduction

The generation of sound by a subsonic jet has resisted any simple mechanistic description. While manipulations of the flow equations can provide a hierarchy of theoretical noise-source definitions (Goldstein 2003), the details of the process are masked in the complexity of the flow turbulence. Even then there is the additional complication that most of the turbulence energy does not directly couple to the sound field: it is the subtle growth and decay of the energetic turbulence structures and their interactions that puts energy into radiation-capable noise-source components

https://doi.org/10.1017/S0022112005007093 Published online by Cambridge University Press

(Ffowcs Williams 1963; Crighton 1975); however they are defined within a particular model. For example, in the simplest model (Lighthill 1952), where propagation is by the stationary-medium scalar wave equation, a mode must have a supersonic phase velocity to radiate. This condition is satisfied by only a small portion of the fluctuation energy in a subsonic jet. Statistical descriptions of theoretical noise sources are complex, and models for them currently lack the fidelity for reliable predictive acoustic modelling of general flows. Even direct numerical simulations (Colonius, Lele & Moin 1997; Freund 2001), though they have been useful for diagnosing aspects of free-shear-flow noise generation and its modelling, have neither illuminated any generally applicable simplifying principles nor pointed to any clear means of noise reduction.

In this paper we devise an approach to study free-shear-flow noise reduction directly. Given a numerical solution of the compressible flow equations, we solve the adjoint of the linearized perturbed equations backward in time to provide the sensitivity of the noise, as defined quantitatively by an appropriate metric, to changes in control actuation. This sensitivity is used to iteratively improve controls for the selected noise-reduction objective. The scheme is formulated mathematically in § 3.

This iterative approach is, however, computationally intense, requiring numerous numerical solutions of the adjoint and flow equations to optimize the controls. For this reason we considered a two-dimensional mixing-layer model of the near-nozzle region of a jet. The details of the mixing layer and its numerical simulation are provided in the following § 2. This flow has several of the salient features of a jet, but can be computed at a fraction of the expense of even a low-Reynolds-number turbulent jet (Freund 2001). It is also easier to interpret certain results for this simplified flow model, though care must be taken in generalizing the specific results to three-dimensional turbulent flows because of their additional complexity.

Clearly, such an iterative scheme is not designed for implementation in hardware, since the iterative process itself requires full knowledge of the unsteady flow field. Instead, we use it to probe the mechanisms of free-shear-flow noise, particularly the noise due to the quasi-two-dimensional (instability-wave-like) flow structures in a turbulent flow, and perhaps most importantly to gauge how much noise reduction can be accomplished with nozzle controls. (How quiet can it be? What type of control is required?) This study is undertaken in § 4, which contains the bulk of this paper's results. Of particular interest are the changes induced by the control. Once the mixing-layer noise is significantly reduced, and it is shown that this results from a genuine change in the flow as a source of sound, we can compare the original noisy flow and its quietened counterpart to illuminate noise mechanisms in a way that has not been possible before.

2. The two-dimensional mixing layer

2.1. *Flow parameters*

The mixing layer simulated is shown schematically in figure 1. The velocity difference across the layer is ΔU, with which we can define the inflow vorticity thickness,

$$\delta_\omega = \frac{\Delta U}{|\mathrm{d}u/\mathrm{d}y|_{\max}}, \tag{2.1}$$

of the initial hyperbolic tangent velocity profile for use as a length scale. This inflow condition simplifies the flow relative to its experimental counterpart by removing any interaction with a splitter plate (or nozzle lip), which can change the character of the

https://doi.org/10.1017/S0022112005007093 Published online by Cambridge University Press

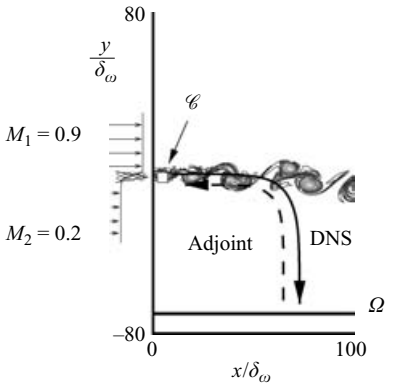


FIGURE 1. Mixing layer control schematic.

acoustic radiation. The flow Reynolds number is $Re_u \equiv \rho_\infty \Delta U \delta_\omega / \mu = 500$ with μ the constant viscosity of the fluid and ρ_∞ the ambient density, which is the same in both streams. We also assume zero bulk viscosity. The Mach numbers of the free streams are $M_1 = U_1/a_\infty = 0.9$ and $M_2 = U_2/a_\infty = 0.2$, where a_∞ is the ambient sound speed. We assume a perfect gas with constant Prandtl number $Pr \equiv c_p \mu / k = 0.7$.

The flow was simulated in a domain extending $100\delta_\omega$ in x and out to $\pm 80\delta_\omega$ in y, as shown in figure 1. The line Ω at $y = -70\delta_\omega$ and extending between $x = 0$ and $x = 100\delta_\omega$ was targeted by our control for noise reduction. This one-sided noise reduction objective is inspired by jet noise reduction, which is most important in the downward toward-the-ground direction, though the formulation admits considerable flexibility in selecting Ω. It is possible to select an Ω in the far field, but computing far-field sound and propagating the adjoint solution back into the meshed computational domain would both introduce errors and add considerable complexity. The computational savings of such an approach would be small because most mesh points are in the vortical region of the flow. The controls discussed subsequently were applied only in the small square region labelled $\mathscr{C}$ in the figure, covering $x/\delta_\omega \in [1, 7]$ and $y/\delta_\omega \in [-3, 3]$. Since $\mathscr{C}$ does not span the entire width of the mixing layer that has significant vorticity (see figure 1), we do not anticipate laminarization to be an option for our control.

2.2. *Governing flow equations*

The compressible viscous flow equations were formulated in Cartesian coordinates and are provided in full in Appendix A. Here, the equations are presented only in operator form. The compressible flow equations are thus

$$\mathscr{N}(\boldsymbol{q}) = \boldsymbol{0}, \tag{2.2}$$

where $\boldsymbol{q}$ is a vector of the primitive flow variables $\boldsymbol{q} = [\rho \;\; u \;\; v \;\; p]^T$.

The control is implemented into the equations as a general source term $\phi(\boldsymbol{x}, t)$ with compact support in $\mathscr{C}$ (see figure 1):

$$\mathscr{N}(\boldsymbol{q}) = \boldsymbol{F}\phi(\boldsymbol{x}, t), \tag{2.3}$$

where the vector $\boldsymbol{F}$ puts the control's action into the different equations that make up $\mathscr{N}$ (see Appendix A) and enforces certain consistencies for the control forcing. For example, it is designed so that momentum forcing appears consistently in the momentum equation and in the total energy equation, where it acts on the kinetic

https://doi.org/10.1017/S0022112005007093 Published online by Cambridge University Press

Source type	(f_1, f_2, f_3, f_4)	(f_1', f_2', f_3', f_4')	(a_2^*, a_3^*)	g
Mass†	$(1, 0, 0, T_0/\gamma)$	$(0, 0, 0, 0)$	$(0, 0)$	$\rho^* + p^* T_0/\gamma$
x body force	$(0, 1, 0, u)$	$(0, 0, 0, u')$	$(p^*, 0)$	$u^* + up^*$
y body force	$(0, 0, 1, v)$	$(0, 0, 0, v')$	$(0, p^*)$	$u^* + up^*$
Int. energy	$(0, 0, 0, 1)$	$(0, 0, 0, 0)$	$(0, 0)$	p^*

†with zero velocity and temperature $T_0 = 1/(\gamma - 1)$

TABLE 1. Vectors used for different controls: $\boldsymbol{F} = [f_1 \ f_2 \ f_3 \ f_4]^T$ defined in (2.3); $\boldsymbol{F}' = [f_1' \ f_2' \ f_3' \ f_4']^T$ defined in (3.7); $\mathscr{A}^* = [0 \ a_2^* \ a_3^* \ 0]^T$ defined in (3.12); and the gradient $g(\boldsymbol{x}, t)$ defined in (3.5).

energy. Specific $\boldsymbol{F}$ vectors for the flow equations in Appendix A are listed in table 1 for the different types of control considered.

2.3. *Numerical methods*

The flow equations were solved numerically and without any modelling approximations. A fourth-order Runge–Kutta algorithm was used to advance the solution in time. Spatial derivatives were computed with a sixth-order compact finite-difference scheme (Lele 1992) in the x-direction and a fourth-order seven-point explicit coefficient-optimized finite-difference scheme (Tam & Webb 1993) in the y-direction. The explicit scheme in y facilitated domain decomposition for solution on parallel computer systems.

In our computation, the equations were discretized with 960×640 mesh points in the x-and y-directions, respectively. The mesh was stretched in y to increase the resolution in the shear layer. It had a minimum spacing $\Delta y_{\min} = 0.14\delta_\omega$ at $y = 0$, a maximum spacing $\Delta y_{\max} = 0.96\delta_\omega$ at $y = \pm 80\delta_\omega$, and a maximum stretching rate $|(\Delta y_{i+1} - \Delta y_i)/\Delta y_i|_{\max} = 1.6\,\%$ at $y \approx \pm 55\delta_\omega$. Beyond the physical domain (see § 2.1), the mesh was stretched continuously and extended $60\delta_\omega$ upstream and downstream of the physical domain in x and $20\delta_\omega$ beyond its top and the bottom in y. In these zones, damping with strength increasing away from the physical domain was added to the equations in order to mimic a radiation condition (Freund 1997). Specifically, the damping terms appear in the governing equations simply as

$$\mathscr{N}(\boldsymbol{q}) = -\xi(\boldsymbol{q} - \boldsymbol{q}_{\text{target}}), \tag{2.4}$$

where the damping coefficient ξ is zero in the physical domain and varies quadratically from 0 to $0.2a_\infty/\delta_\omega$ between the physical and the computational domain boundaries. By the time all fluctuations reached the actual boundaries of the computational domain, they were reduced to such a negligible level that standard one-dimensional characteristic boundary conditions adequately absorbed outgoing perturbations.

2.4. *Inflow excitation*

To make the mixing layer well-defined and reproducible and to avoid any spurious auto-excitation associated with the numerical discretization, we explicitly excited our mixing layer. Another objective of this excitation was to provide a relatively high amplitude disturbance level at the inflow to properly challenge the controller.

Linear instability analysis predicts that the most unstable mode of the corresponding incompressible mixing layer, with the assumption of parallel flow, has Strouhal number $St_0 = f_0\delta_\omega/(4U_c) \approx 0.032$ (Monkewitz & Huerre 1982), where $U_c = (U_1 + U_2)/2$ and f_0 is the mode frequency. Thus, frequency f_0 provides an estimate of

https://doi.org/10.1017/S0022112005007093 Published online by Cambridge University Press

the fundamental frequency of our compressible mixing layer, since it is not very sensitive to the present compressibility level (Sandham & Reynolds 1991). Numerical experimentation confirmed that our mixing layer does respond most strongly to excitations with frequencies near f_0.

We excited the flow at a total of eight frequencies,

$$f_i = \frac{f_0}{4}\left(i + \alpha^{(i)}\right), \quad i = 1,\ 2,\ \ldots,\ 8, \tag{2.5}$$

where $\alpha^{(i)}$ are uniformly distributed random numbers such that $\alpha^{(i)} \in (-0.5, 0.5)$. In §4.1, we confirm that the noise and its controllability are insensitive to the particular random numbers defining the excitation. For comparison, we also simulated and controlled a mixing layer excited with f_0, $2f_0$, and 6 subharmonics of f_0. This excitation, which is similar to that used by Colonius *et al.* (1997), produces a regular roll-up and pairing of vorticies (see §4.6).

A special procedure was designed to reduce the direct effect of the excitation on the sound field. We defined

$$\psi = \psi_0\, \mathrm{e}^{-0.2(x-x_0)^2} \mathrm{e}^{-0.2y^2} \sum_{i=1}^{8} \sin\left[\frac{2\pi f_i (x - x_0 - U_c t)}{U_c} + \beta_x^{(i)}\right] \sin\left[\frac{2\pi f_i\, y}{U_c} + \beta_y^{(i)}\right], \tag{2.6}$$

where $\psi_0 = 0.008\rho_\infty a_\infty^2/\delta_\omega$ and $x_0 = -10\delta_\omega$. The β_x and β_y are random phases $\in [0, 2\pi)$ and are constant for the entire simulation. The excitation was then included as a body force

$$\boldsymbol{F}_e = \left(\frac{\partial \psi}{\partial y}, -\frac{\partial \psi}{\partial x}\right), \tag{2.7}$$

which is solenoidal and thus relatively quiet. Our selected x_0 puts the excitation upstream of the physically realistic portion of the computation. The ξ in (2.4) has maximum value of only $0.0125a_\infty/\delta_\omega$ in this region, which does counteract the excitation but does not significantly interfere with its objectives.

This approach can generate disturbances at the physical domain boundary that are higher amplitude than could be accurately prescribed locally at the inflow boundary without generating spurious sound. The average turbulence intensity at the centre of the control region ($x = 4\delta_\omega$, $y = 0$) close to the inflow was already 70 % of its peak value further downstream. The excitation $\boldsymbol{F}_e$ appears in the momentum equations, but has support only for $x < 0$, which is the beginning of what we consider the physical domain. Therefore, for clarity we omit it from subsequent analysis. Its purpose is solely to provide an inflow condition. Our controller, of course, has no direct knowledge of this excitation. Because the base flow is a slowly spreading shear layer, the noise from the excitation is not expected to be exactly zero, but both visualizations and the eventual success of the control show that it is negligible relative to the physical noise from the mixing layer.

2.5. *Simulation procedure*

To avoid initial transients, we first simulated the flow for time $588\delta_\omega/\Delta U$, which is approximately 59 fundamental vortex roll-up periods according to our estimated f_0. This process took 10 500 numerical time steps with $\Delta t = 0.056\delta_\omega/\Delta U$. Then the control was applied for $437.5\delta_\omega/\Delta U$ time units, which is about 44 fundamental roll-up periods. Figure 2(*a*) shows the flow and sound fields, which include data in two regions: the direct numerical simulation data (inner area) and a far-field acoustic extrapolation beyond the simulation domain, which was computed as by Freund

https://doi.org/10.1017/S0022112005007093 Published online by Cambridge University Press

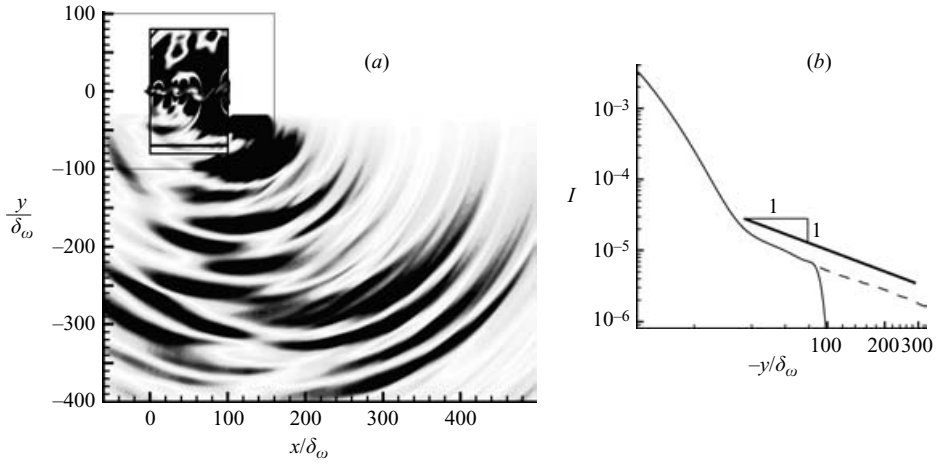


FIGURE 2. (*a*) Visualization of the flow and sound field before control. The rectangular boxes outline the physical and total (including boundary zones) computational domains. (*b*) Sound intensity $I = \overline{(p-\bar{p}_o)^2}/\rho_\infty^2 a_\infty^4$ on $x = 94\delta_\omega$: flow simulation data (———) (the sudden drop near $x = 100\delta_\omega$ corresponds to the absorbing boundary zone) and acoustic extrapolation data (– – – –).

(2001) using pressure data at $y = -30\delta_\omega$. It is seen in figure 2(*b*) that the target line Ω at $y = -70\delta_\omega$ is indeed in the far acoustic field, as defined for this purpose by a $1/r$ intensity decay. This supports our approach of using the pressure data on Ω to control the far-field sound.

3. Control formulation

3.1. *The control and its objective*

The control objective is to make the mixing layer as quiet as possible with local actuation near the inflow, which will allow us to study noise mechanisms effectively and establish an empirical lower bound on the mixing-layer noise. Thus, it is desirable to have the most general control possible, which in our simulation methodology corresponds to treating each space–time point of the discrete representation of $\phi(\boldsymbol{x}, t)$ in (2.3) as an independent control parameter. In the reported results, the function ϕ is discretized over a 36×45 point subregion of the simulation mesh in $\mathscr{C}$ for 7812 time steps, giving approximately 10^7 control parameters to be optimized. (The much smaller number of control dimensions actually necessary for control is investigated in § 4.5.)

The control's specific objective is to reduce noise as defined by the cost functional

$$\mathscr{J}(\phi) = \int_{t_0}^{t_1}\int_{\Omega} [p(\phi(\boldsymbol{x}, t), \boldsymbol{x}, t) - \bar{p}_o(\boldsymbol{x})]^2 \,\mathrm{d}\boldsymbol{x}\,\mathrm{d}t, \tag{3.1}$$

where t_0 and t_1 are the start and end times of the control period, p is the local pressure, which can be viewed as depending upon the control $\phi(\boldsymbol{x}, t)$, and $\bar{p}_o$ is the spatially dependent but time-averaged pressure before control is applied. This mean pressure is nearly uniform on Ω with $|\bar{p}_o - p_\infty| < 0.0017 p_\infty$, where p_∞ is the nominal ambient pressure, but since this variation is comparable with the uncontrolled acoustic pressure fluctuations ($\approx 0.003 p_\infty$), this difference of the mean pressure from the pressure at infinity is important for properly defining the sound. The mean pressure of the

https://doi.org/10.1017/S0022112005007093 Published online by Cambridge University Press

controlled cases, $\bar{p}$, is not constrained, and in principle can drift due to the control, though any such drift would be penalized by increasing $\mathscr{J}$. We observe, however, that the difference in $\bar{p}$ from $\bar{p}_o$ on Ω is less than 3 % of the maximum uncontrolled acoustic pressure fluctuations, so $\mathscr{J}(\phi)$ in (3.1) effectively remains acoustic when control is applied.

3.2. *Sensitivity*

To determine the sensitivity of the cost functional $\mathscr{J}$ to small modifications of the control ϕ, we consider the perturbation $\mathscr{J}'$ that results from an arbitrary perturbation ϕ' to the control ϕ. This perturbation $\mathscr{J}'$ is defined as a differential of the cost functional $\mathscr{J}$ with respect to $\phi(\boldsymbol{x}, t)$ in the direction ϕ':

$$\mathscr{J}' \equiv \lim_{\varepsilon \to 0} \frac{\mathscr{J}(\phi + \varepsilon\phi') - \mathscr{J}(\phi)}{\varepsilon} = \int_{t_0}^{t_1} \int_{\Omega} 2[p(\phi, \boldsymbol{x}, t) - \bar{p}_o(\boldsymbol{x})] p'(\boldsymbol{x}, \phi, \phi') \, \mathrm{d}\boldsymbol{x} \, \mathrm{d}t. \quad (3.2)$$

The limit that defines p' in the integrand is exactly analogous to that which defines $\mathscr{J}'$. In forming the rightmost term in (3.2) from (3.1), the derivative operation can be viewed as commuting with the integration operation. With the differential of the functional $\mathscr{J}$ defined in (3.2), the gradient $g(\phi)$ of the functional $\mathscr{J}$ for any direction ϕ' can be defined implicitly as (Vainberg 1964)

$$\mathscr{J}' = \int_{t_0}^{t_1} \int_{\mathscr{C}} g(\phi)\phi' \, \mathrm{d}\boldsymbol{x} \, \mathrm{d}t. \quad (3.3)$$

The space integration in (3.3) is only over $\mathscr{C}$, the support of ϕ'. Together (3.2) and (3.3) provide an implicit formula for g,

$$\int_{t_0}^{t_1} \int_{\mathscr{C}} g(\phi)\phi' \, \mathrm{d}\boldsymbol{x} \, \mathrm{d}t = \int_{t_0}^{t_1} \int_{\Omega} 2[p(\phi, \boldsymbol{x}, t) - \bar{p}_o(\boldsymbol{x})] p'(\boldsymbol{x}, \phi, \phi') \, \mathrm{d}\boldsymbol{x} \, \mathrm{d}t, \quad (3.4)$$

which in principle could be solved for the best ϕ' if all p' were known for all potential ϕ' perturbations, but to solve for the n space–time components of ϕ', we would need to solve the flow at least n times for n linearly independent perturbations. For large n (10^7 in our case), this option is impractical. In the next section, we use an adjoint formulation to solve for g directly, which can then be used to update the control by

$$\phi^{\mathrm{new}} = \phi^{\mathrm{old}} - r g(\phi^{\mathrm{old}}), \quad (3.5)$$

where r is a generalized distance in ϕ-coordinates determined iteratively to minimize $\mathscr{J}(\phi^{\mathrm{new}})$ in the g-direction.

3.3. *Adjoint-based optimization: formulation*

Our formulation is similar to that of Bewley, Moin & Temam (2001) for incompressible flow and we use similar notation. As in (3.2), a differential is applied to all flow variables $\boldsymbol{q}$, to define $\boldsymbol{q}' = [\rho' \quad u' \quad v' \quad p']^T$. We take $\boldsymbol{q}'$ to be the still unknown perturbation to a solution $\boldsymbol{q}$ of the flow equations (2.3) due to a control perturbation ϕ', though this specific designation is not assumed by the differential definition of $\boldsymbol{q}'$. Mathematically, this means that

$$\mathscr{N}(\boldsymbol{q} + \boldsymbol{q}') = \boldsymbol{F}(\boldsymbol{q} + \boldsymbol{q}')(\phi + \phi'), \quad (3.6)$$

where the notation for the term on the right-hand side indicates that the vector $\boldsymbol{F}$ depends on $\boldsymbol{q} + \boldsymbol{q}'$ and multiplies the scalar $\phi + \phi'$. Linearizing (3.6) in $\boldsymbol{q}'$, or equivalently taking the differential of the governing equation (2.3), yields

$$\mathscr{N}'(\boldsymbol{q})\boldsymbol{q}' = \boldsymbol{F}'\phi + \boldsymbol{F}\phi'. \quad (3.7)$$

https://doi.org/10.1017/S0022112005007093 Published online by Cambridge University Press

The operation $\mathscr{N}'(\boldsymbol{q})\boldsymbol{q}'$ is linear in $\boldsymbol{q}'$, though $\mathscr{N}'(\boldsymbol{q})$ is itself a nonlinear function of $\boldsymbol{q}$. It is convenient for the subsequent development to define

$$\mathscr{M}'(\boldsymbol{q},\phi)\boldsymbol{q}' = \mathscr{N}'(\boldsymbol{q})\boldsymbol{q}' - \boldsymbol{F}'\phi = \boldsymbol{F}\phi', \tag{3.8}$$

thus isolating the control perturbation on the right-hand side of the equation. The $\boldsymbol{F}'$ corresponding to the specific controls we consider are listed in table 1.

With an inner product defined

$$\langle \boldsymbol{c}, \boldsymbol{d}\rangle \equiv \int_{t_0}^{t_1}\int_{\mathbb{R}^2} \boldsymbol{c}\cdot\boldsymbol{d}\,\mathrm{d}\boldsymbol{x}\,\mathrm{d}t \equiv \int_{t_0}^{t_1}\int_{\mathbb{R}^2}\sum_{n=1}^{4} c_n(\boldsymbol{x},t)d_n(\boldsymbol{x},t)\,\mathrm{d}\boldsymbol{x}\,\mathrm{d}t, \tag{3.9}$$

the adjoint of $\mathscr{M}'(\boldsymbol{q})$ is obtained by integration by parts:

$$\langle \mathscr{M}'(\boldsymbol{q})\boldsymbol{q}', \boldsymbol{q}^*\rangle = -\langle \boldsymbol{q}', \mathscr{M}^*(\boldsymbol{q})\boldsymbol{q}^*\rangle + b, \tag{3.10}$$

where b includes the space and time boundary terms (see equation (3.13) below) and

$$\boldsymbol{q}^* = [\,\rho^* \;\; u^* \;\; v^* \;\; p^*\,]^T \tag{3.11}$$

is introduced as the adjoint field. The adjoint operator $\mathscr{M}^*$ includes two parts:

$$\mathscr{M}^*(\boldsymbol{q})\boldsymbol{q}^* = \mathscr{N}^*(\boldsymbol{q})\boldsymbol{q}^* + \mathscr{A}^*(\boldsymbol{q}^*)\phi. \tag{3.12}$$

The term $\mathscr{A}^*(\boldsymbol{q}^*)$ arises from $\boldsymbol{F}'$ in (3.8) and is non-zero only for certain cases, as indicated in table 1. The term $\mathscr{N}^*(\boldsymbol{q})\boldsymbol{q}^*$ is derived from the flow equations (see Appendix B) and is the same for all controls considered.

The boundary term b in (3.10) is

$$b = \iint_{t_0}^{t_1} (\boldsymbol{B}_x\,\boldsymbol{q}')\cdot\boldsymbol{q}^*\Big|_{x=-\infty}^{x=+\infty}\mathrm{d}t\,\mathrm{d}y + \iint_{t_0}^{t_1} (\boldsymbol{B}_y\,\boldsymbol{q}')\cdot\boldsymbol{q}^*\Big|_{y=-\infty}^{y=+\infty}\mathrm{d}t\,\mathrm{d}x + \int_{\mathbb{R}^2} (\boldsymbol{B}_t\,\boldsymbol{q}')\cdot\boldsymbol{q}^*\Big|_{t_0}^{t_1}\mathrm{d}\boldsymbol{x}, \tag{3.13}$$

where the $\boldsymbol{B}$ factors are 4×4 matrices. This boundary term b can be eliminated by choosing appropriate boundary and initial conditions for the adjoint problem. Mathematically, causality ensures that the first two integrals are zero for the finite time interval considered here. However, since the physical domain of the computation was necessarily finite, an effectively equivalent radiation-like condition was enforced at the numerical boundary. This condition was implemented in practice as in the flow solution with a combination of characteristic boundary conditions and an absorbing boundary zone. Causality also eliminates the time boundary term at the initial time $t = t_0$ in the third integral: there can be no perturbation to the flow (i.e. $\boldsymbol{q}' = 0$) due to the control before the control is applied. The condition at the end time $t = t_1$ can be eliminated by simply starting with $\boldsymbol{q}^* = 0$ at $t = t_1$ and solving the adjoint system backward in time.

We can now choose a source term $\boldsymbol{F}^*$ for our adjoint system,

$$\mathscr{M}^*(\boldsymbol{q})\boldsymbol{q}^* = \boldsymbol{F}^*, \tag{3.14}$$

so that the adjoint solution provides the gradient g in (3.5). We start by substituting (3.8) and (3.14) into (3.10) with $b = 0$ as discussed to show that

$$\langle \boldsymbol{F}\phi', \boldsymbol{q}^*\rangle = -\langle \boldsymbol{q}', \boldsymbol{F}^*\rangle. \tag{3.15}$$

Comparing (3.15) with (3.4), we would like to obtain

$$-\langle \boldsymbol{q}', \boldsymbol{F}^*\rangle = \int_{t_0}^{t_1}\int_{\Omega} 2[p(\phi,\boldsymbol{x},t) - \bar{p}_o(\boldsymbol{x})]\,p'(\boldsymbol{x},\phi,\phi')\,\mathrm{d}\boldsymbol{x}\,\mathrm{d}t, \tag{3.16}$$

https://doi.org/10.1017/S0022112005007093 Published online by Cambridge University Press

so that

$$\langle \boldsymbol{F}\phi', \boldsymbol{q}^* \rangle = \int_{t_0}^{t_1} \int_{\mathscr{C}} g(\phi)\phi' \, \mathrm{d}\boldsymbol{x} \, \mathrm{d}t. \tag{3.17}$$

The adjoint source term $\boldsymbol{F}^*$ that gives (3.16) from (3.9) is

$$\boldsymbol{F}^* = \left[0 \quad 0 \quad 0 \quad -2(p - \bar{p}_o) \int_{\Omega} \delta(\boldsymbol{x} - \boldsymbol{x}_o) \, \mathrm{d}\boldsymbol{x}_o \right]^T, \tag{3.18}$$

and by (3.17)

$$g(\phi) = \boldsymbol{F} \cdot \boldsymbol{q}^*, \tag{3.19}$$

where, in practice, q^* is known from the numerical solution of the adjoint system and $\boldsymbol{F}$ is case dependent and defined in table 1. With $g(\phi)$, we now have the generalized direction in which to change ϕ to reduce $\mathscr{J}$ for use in a gradient-based optimization procedure.

3.4. *Adjoint-based optimization: numerical implementation*

The adjoint equations are solved on the same mesh and by the same methods used to solve the flow equations. The δ-function in (3.18) is distributed to the computational mesh by a Gaussian distribution function $\exp(-(y + 70\delta_\omega)^2/(4\Delta y^2))$, where Δy is the local mesh spacing. Thus, our smeared out approximation to the δ-function has width $\approx 2.7\delta_\omega$, which is much less than the wavelength ($\gtrsim 14\delta_\omega$) of any significant radiated sound waves. This was proved to be effective in noise cancellation tests (Wei 2004).

For the control update, the Polak–Ribiere variant of the conjugate gradient algorithm is used with Brent's line minimization (Press *et al.* 1986). Each line minimization typically required approximately 10 flow solutions and 10 adjoint solutions. One entire line-minimization procedure, which accomplishes the step along one conjugate gradient, is designated as one iteration in the following, so the number of field solutions can be estimated as $\approx 20\times$ (# iterations), but this approximate number is, of course, sensitive to the local shape of $\mathscr{J}(\phi)$. All optimizations were started from a $\phi = 0$ condition, which may be responsible for the particular optimized conditions found by the control because standard gradient descent searches can only find local minima. Since the success of our control is sufficient to study noise mechanisms of interest, we have not investigated this possibility.

As shown in § 3.3, the entire flow-field solution needs to be saved in order to solve the adjoint equations. To save memory and minimize data input and output operations, we saved the flow solutions only at every other point in space and time and interpolated using third-order polynomials in space and linear interpolation in time. No differences were noted between test cases computed used the full fields and the interpolated fields. The optimizations presented in this paper each required approximately 20 000 processor-hours of computation on an IBM SP3, usually using 80 processors and requiring about 30 gigabytes of memory.

3.5. *Adjoint solution*

The evolution of the adjoint pressure p^* is visualized in figure 3. It is this quantity that provides the gradient information g to update the internal-energy control and is a factor in all the types of control studied (see table 1). Since the flow equations are self-adjoint in the acoustic limit, the adjoint pressure starts as an adjoint sound wave, excited along Ω by the pressure as specified in (3.18). When this wave encounters the mixing layer, it excites disturbances that convect upstream in the shear layer in a way similar (but time reversed) to the motion of the vortex structures of the flow field,

https://doi.org/10.1017/S0022112005007093 Published online by Cambridge University Press

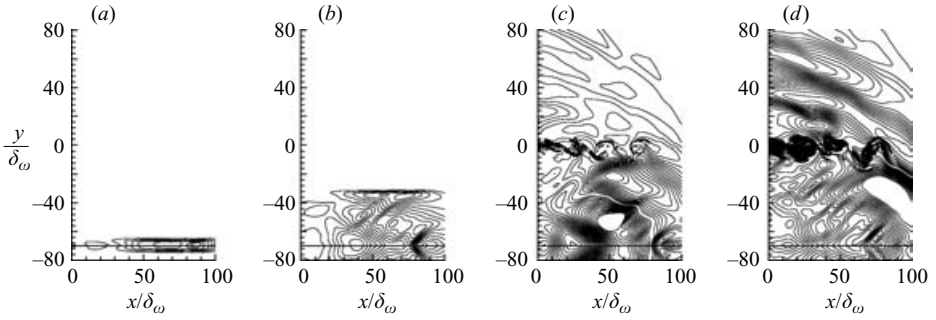


FIGURE 3. Adjoint pressure p^*: (*a*) $t = 435.1\delta_\omega/\Delta U$, (*b*) $t = 411.6\delta_\omega/\Delta U$, (*c*) $t = 294\delta_\omega/\Delta U$, (*d*) $t = 235.2\delta_\omega/\Delta U$. The time decreases in the adjoint solution.

and with approximately the same speed as the structure convective Mach number, $M_c = 0.55$. These disturbances eventually reach $\mathscr{C}$, where the adjoint solution provides the gradient g to update ϕ according to (3.19). These observations suggest that the effect of the control follows the same track but in reverse from $\mathscr{C}$ to the target line Ω. They also suggest that the control mechanism is via the instabilities and flow structures in the mixing layer, and not so-called anti-sound acoustic cancellations, an issue that is revisited in detail in § 4.2. Given this qualitative behaviour of the adjoint, we can express the expected mechanism of noise control as follows: (i) the control interacts with the flow, (ii) this interaction alters (slightly, as we shall see) the instabilities in the flow, and (iii) the modified flow is quieter. This interpretation will be strengthened quantitatively in § 4.

3.6. *Price term*

It should be noted that the cost $\mathscr{J}$ in (3.1) does not penalize the control effort. A term to do this was intentionally omitted since our primary objective is to study the effect of the control on the flow and its noise mechanism, not to seek any mathematically formal optimum. Such an objective would probably require a price term added to (3.1) that penalizes the control effort:

$$\mathscr{H}(\phi) = \mathscr{J}(\phi) + c_w \int_{t_0}^{t_1} \int_{\mathscr{C}} \phi^2 \, \mathrm{d}\boldsymbol{x} \, \mathrm{d}t. \tag{3.20}$$

The gradient to reduce $\mathscr{H}$ is then

$$g(\phi) = \boldsymbol{F} \cdot \boldsymbol{q}^* + 2c_w\phi. \tag{3.21}$$

Numerical results for this formulation are provided by Wei (2004). Though the control effectiveness is, of course, reduced for large enough c_w, all of the following conclusions are unchanged by the price term. Pertinent observations on the price term's effect are noted in the following. In § 4.3, we will briefly discuss its effect on the spectrum of the control and in § 4.4 we will mention that it is responsible for increasing the streamwise integral length scale of the control.

4. Results

4.1. *Sound reduction*

Figure 4 shows the reduction of $\mathscr{J}$ by different types of control. To make this plot, we defined the starting point t_0 in the cost function (3.1) as the acoustic travel time from

https://doi.org/10.1017/S0022112005007093 Published online by Cambridge University Press

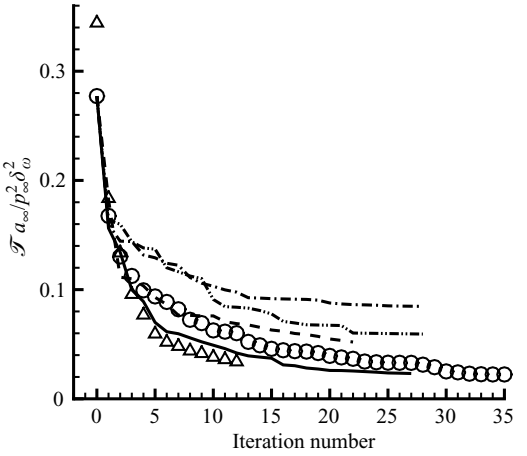


FIGURE 4. The reduction of the cost function by different controls: mass (–··–··); x-direction body force (– – – –); y-direction body force (–·–·–); internal energy (———); and all-terms control (◯). The △ show internal energy control for the same flow but with different random number excitation in (2.5) and (2.6).

$\mathscr{C}$ to the nearest point on Ω. This approximation provides a lower bound on the time at which the control will be effective on Ω. Before this time, $\mathscr{J}$ not reducible from $\mathscr{C}$, but even for a period after this adjusted t_0, the sound on Ω is not fully controllable for two reasons: (i) the control's effect can only reach the closest point on Ω, and (ii) the rate at which the control's effect travels within the mixing layer is slower than the sound speed. In the layer, it is expected to travel at approximately the structure convective Mach number, $M_c \approx 0.55$, as suggested by the adjoint solution behaviour seen in § 3.5. With this definition, all controls reduced the noise on the target line by more than 60 %, with the internal-energy control showing a 92 % (11 dB) sound reduction. A case with the mixing layer excited by a different set of random numbers $\alpha^{(i)}$ is also shown in this figure to demonstrate insensitivity to the specifics of the artificial random excitation.

We also tried to maximize controllability by combining all four types of control simultaneously. In this case, the control space is 4 times larger than the original one, so we generalize the control to be $\phi_i(\boldsymbol{x}, t)$ for $i = 1, 2, 3, 4$ and use corresponding $\boldsymbol{F}_i$ to represent each of the $\boldsymbol{F}$ vectors in table 1, so (2.3) becomes

$$\mathscr{N}(\boldsymbol{q}) = \sum_{i=1}^{4} \boldsymbol{F}_i \phi_i(\boldsymbol{x}, t). \tag{4.1}$$

The corresponding cost-function reduction is also shown in figure 4. It is decreased more slowly for the selected optimization parameters than, say, the internal-energy control only, but eventually it approaches about the same control effectiveness. (No attempt was made here or throughout to attach any particular significance to the rate of convergence.) Since the all-terms control offered no clear benefit, we do not discuss it in the rest of this paper and study the four single-equation control types separately.

The sound further from the mixing layer has, of course, been reduced as well, mostly in, but not limited to, the sideline direction targeted by the selected Ω. Figure 5 shows the initial and controlled directivity on a circular arc centred at $x = 50\delta_\omega$ and $y = 0$

https://doi.org/10.1017/S0022112005007093 Published online by Cambridge University Press

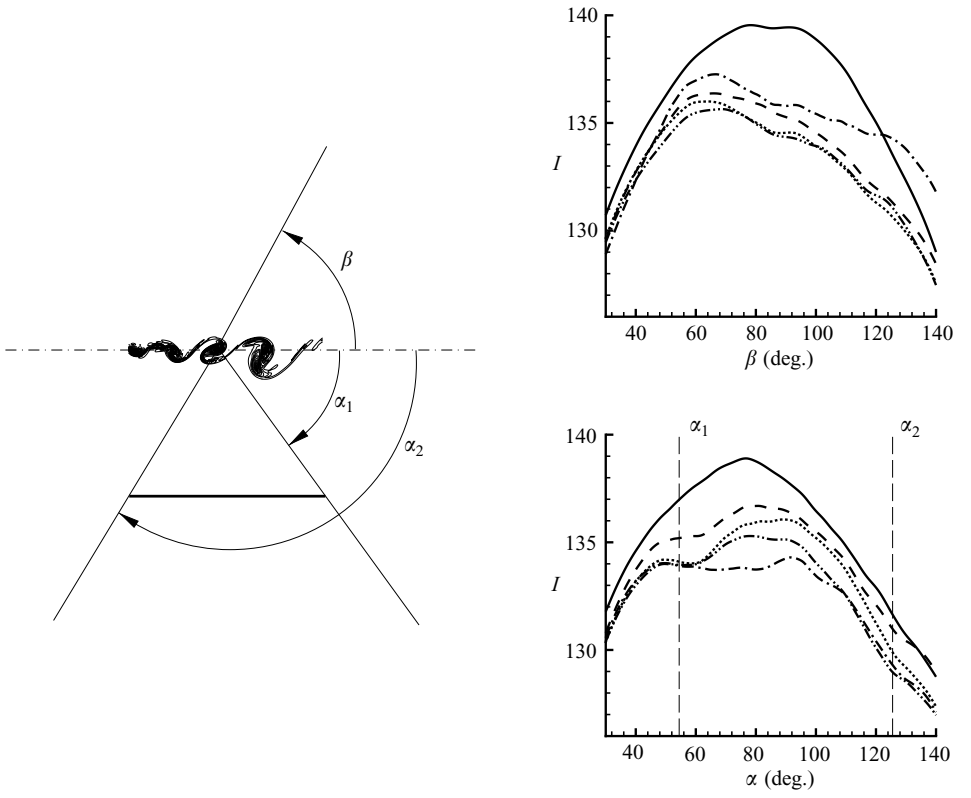


FIGURE 5. Sound directivity: without control (———); and with mass (·····), x-direction body force (–··–··), y-direction body force (– – – –), and internal energy (–·–·–) controls.

with radius $R = 300\delta_\omega$. The greatest reduction is in the acoustic shadow of Ω, between $\alpha = 54^\circ$ and 126°. For smaller and larger α, the control's effectiveness is diminished, though the noise is still reduced. Intensity at angles $\alpha, \beta < 40^\circ$ and $> 140^\circ$ were not computed because they were determined by testing with known sources to be inaccurate in the far field. Surprisingly, the noise is reduced at all angles, even in the opposite direction to that targeted by our choice of Ω. This overall reduction is inconsistent with any simple anti-sound noise cancellation mechanisms, which is investigated in detail next.

4.2. *Anti-sound?*

Before proceeding to investigate the effects of the control on the flow, it is important to establish quantitatively that the noise reduction is indeed by a change in the flow as a source of sound and not an anti-sound acoustic cancellation with ϕ in $\mathscr{C}$ providing the cancelling acoustic waves. It has already been suggested in § 3.5 that since adjoint instability waves dominate the gradient information in $\mathscr{C}$, the control mechanism should be linked to the hydrodynamics.

To demonstrate further that our control is not by anti-sound and is, in fact, far superior to what could be accomplished with anti-sound, we designed the numerical experiment shown in figure 6(*a*). Here, $\mathscr{C}$ is moved away from the shear layer such that it is now defined by $x/\delta_\omega \in [1, 7]$ and $y/\delta_\omega \in [-21, -15]$. The adjoint instability wave never reaches this control region, so control should be principally by acoustic cancellation. Only the internal-energy source control, which can be an

https://doi.org/10.1017/S0022112005007093 Published online by Cambridge University Press

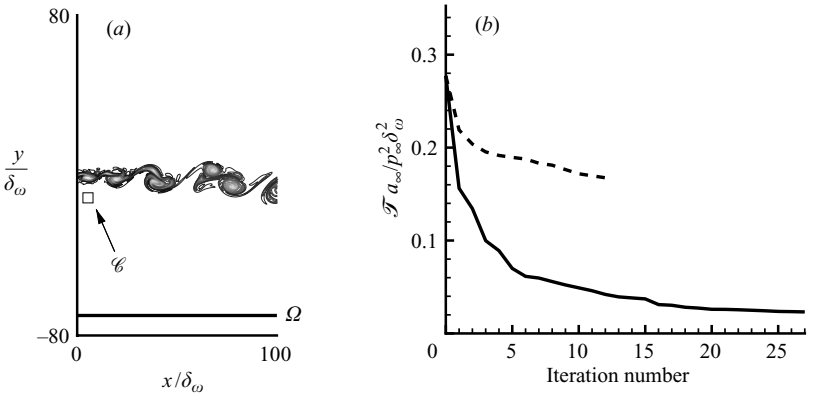


FIGURE 6. Anti-sound control test: (*a*) configuration schematic; (*b*) the reduction of $\mathscr{J}$ by internal energy source control in the shear layer (———) (from figure 4) and off the shear layer (– – – –).

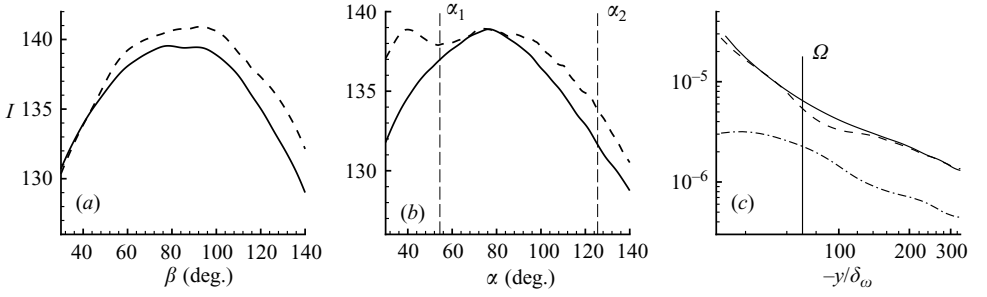


FIGURE 7. (*a*, *b*) Sound directivity: without control (———) and with internal energy anti-sound control (– – – –), with α and β defined in figure 5. (*c*) Sound intensity on the line $x = 94\delta_\omega$: without control (———), with anti-sound control (– – – –), and with internal energy control in the shear layer (– · – · –).

efficient monopole-like sound source, is presented here for demonstration purposes. After 12 iterations, a 40 % reduction is observed (figure 6*b*), which is not surprising because anti-sound is known to be effective locally, though it is also known to increase the sound elsewhere. Figures 7(*a*) and 7(*b*) show the sound directivity of this case. The anti-sound control case is actually louder than the case without control in most directions. Even for the area in the acoustic shadow of Ω, there is no far-field sound reduction. Figure 7(*c*) suggests that the non-collocated flow and control noise sources produce local cancellation on Ω but not beyond. Clearly, the flow control is more effective than would seem possible for just anti-sound, though we cannot rule out the possibility that an anti-sound mechanism might aid it. We saw in figure 5 that the control is not as successful in the far field as on Ω, which suggests that the noise reduction on Ω might indeed include some anti-sound component.

4.3. *Spectra*

There are four important spectra in our controlled flow. The first is of our randomized excitation based on the estimated fundamental frequency f_0, as described in § 2.4. Unless otherwise noted, the particular random numbers used gave excitation frequencies $0.36f_0$, $0.40f_0$, $0.69f_0$, $0.99f_0$, $1.28f_0$, $1.57f_0$, $1.86f_0$, and $1.90f_0$. The second is the spectrum of the optimized control; the third is the near-field spectrum

https://doi.org/10.1017/S0022112005007093 Published online by Cambridge University Press

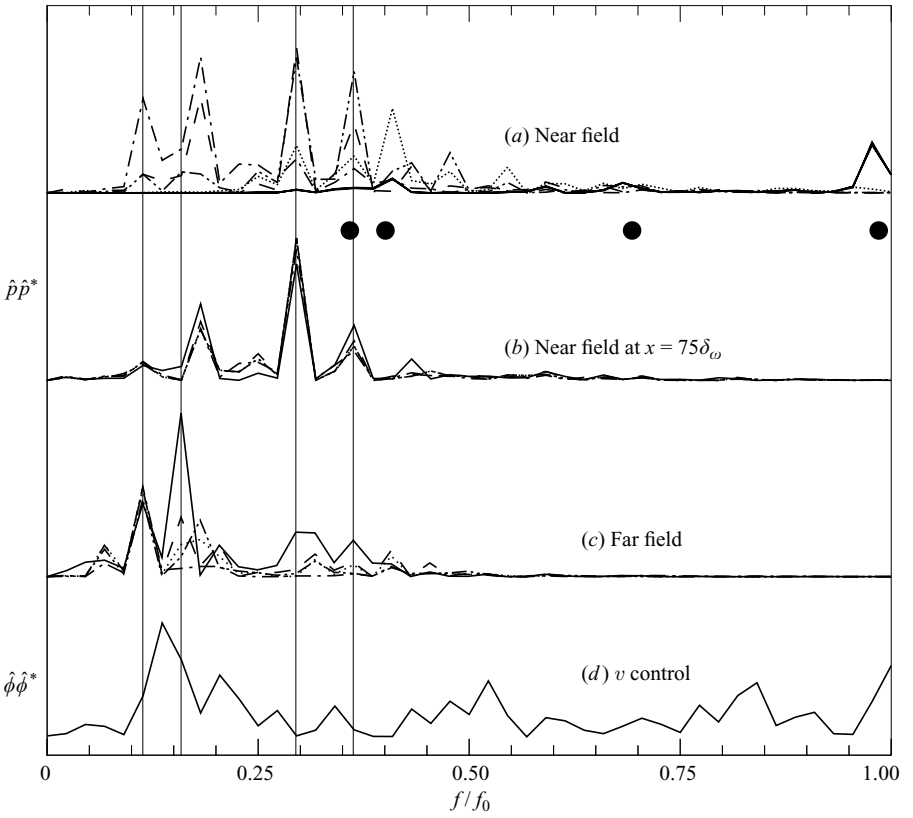


FIGURE 8. Flow and control spectra. (*a*) Near-field ($y = 0$) pressure spectra $\hat{p}\hat{p}^*$. ———, The overlaid controlled cases and uncontrolled cases at $x = 4\delta_\omega$, the centre of $\mathscr{C}$. The no control case is also shown at $x = 25\delta_\omega$ (·····), $x = 50\delta_\omega$ (–··–··), $x = 75\delta_\omega$ (– – – –), and $x = 100\delta_\omega$ (–·–·–). (*b*) Pressure spectra $\hat{p}\hat{p}^*$ at $x = 75\delta_\omega$, $y = 0$ without control (———); and with mass (·····), x-direction body force (–··–··), y-direction body force (– – – –), and internal energy (–·–·–) controls. The same cases are shown with the same line types in (*c*) for the far-field sound pressure spectra $\hat{p}\hat{p}^*$ at $x = 152.6\delta_\omega$, $y = -281.9\delta_\omega$ ($\alpha = -70°$ on the same arc as in figure 5, which is near the angle of maximum intensity). (*d*) The spectrum of the optimized y-direction body-force control $\hat{\phi}\hat{\phi}^*$ at $x = 4\delta_\omega$, $y = 0$. Other controls show similar behaviour. For reference, the filled circles mark the four lowest excitation frequencies. The vertical scale is linear but arbitrary for each set of spectra. Curve sets (*a–c*) are nearly flat for $f > f_0$.

of the mixing layer before and after control is applied; and the fourth is the spectrum of radiated sound before and after control. Figure 8 shows all these spectra.

At the centre of $\mathscr{C}$, just downstream of the random excitation, the dominant frequency is near f_0 (see the curves in figure 8*a*), apparently a direct response to the randomly selected $0.99f_0$ excitation. The control is seen to have an imperceptible effect upon the pressure spectra in $\mathscr{C}$, showing its weak effect on the hydrodynamics. Downstream, dominant frequencies are lower as expected, and more sensitive to the control as seen in figure 8(*b*), though the modest changes observed do not suggest any fundamental change to the flow. It is also noteworthy that the near-field spectrum at $x = 75\delta_\omega$ is dominated by frequencies that are significantly lower than the excitation frequencies, suggesting that nonlinear interactions are responsible for their character.

The optimized control (figure 8*d*) has energy over a wide range of frequencies, not just near the sound frequencies it is designed to control. This observation suggests that

https://doi.org/10.1017/S0022112005007093 Published online by Cambridge University Press

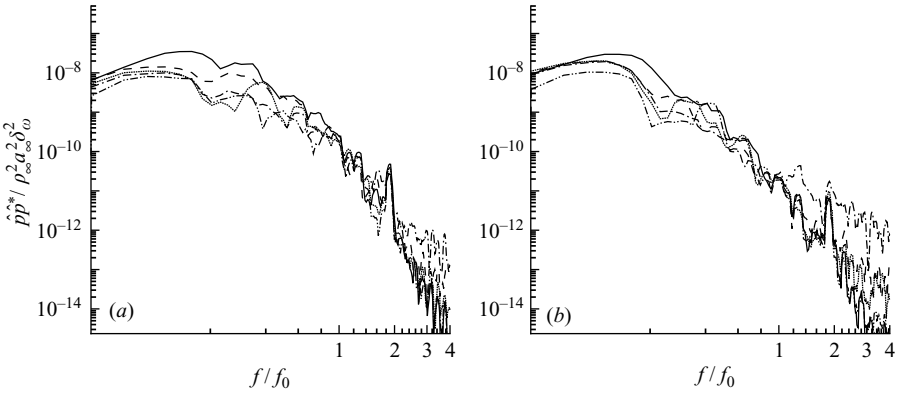


FIGURE 9. Sound pressure spectra on the same arc as in figure 5 at (*a*) $\alpha = 50^\circ$ and (*b*) $\alpha = 90^\circ$: without control (———); and with mass (·····), x-direction body force (–··–··), y-direction body force (– – – –), and internal energy (–·–·–) control.

the control works through the nonlinear dynamics in the mixing layer, not by simply exciting a linear instability that somehow cancels the physical noise, for example. Adding a price term to the cost functional, as discussed in § 3.6, reduced the control's amplitude at all frequencies, suggesting that they are all important.

The far-field noise spectra are significantly changed by the control. Interestingly, all controls seem to affect spectra in about the same way, reducing mainly a particularly loud peak at $f \approx 0.159 f_0$. This peak corresponds to neither a spectral peak in the near-field pressure nor a clear spectral peak in the optimized control. The changes to the complete far-field noise spectrum by different controls are more clearly represented in figure 9. The effect of all controls is to reduce the noise of lower frequencies, which contain most of the acoustic energy, with greater reduction noted closer to the downstream axis. We also see, however, that more high-frequency noise is radiated by the controlled cases. The internal-energy control caused the greatest increase in high frequencies, though it also reduced the overall noise the most.

The apparent success of the controls at some sound frequencies but not others is investigated further in figure 10, which shows directivities in narrow frequency bands for all cases. We see again that the sound is most reduced near the frequency $0.159 f_0$, which is the loudest in the uncontrolled case. It is also seen in figure 10(*b–d*) that the controls are extremely successful at certain angles so that relatively silent angles are formed, suggesting some higher degree of cancellation in the sound source. A similar angle of extinction has been predicted by Huerre & Crighton (1983) for the sound produced by the amplification and decay of instability waves in the shear layers of a jet, and was observed experimentally in Bridges & Hussain (1992)'s round jet experiment and in simulations of regularly forced two-dimensional (Colonius *et al.* 1997) and axisymmetric (Mitchell, Lele & Moin 1999) free shear flows. In all these cases, the flows were excited with a single-frequency or several harmonics. Our randomly excited flow shows no such angles of extinction, and it is well-known that turbulent jets do not either. This is the first indication of several that we will investigate in the remainder of the paper that the control has induced a subtle ordering, which, at least as far as acoustics are concerned, shares characteristics with idealized or regularly forced flows.

We can make a preliminary assessment of this suggested similarity by comparing the control of the randomly excited mixing layer to that of the corresponding harmonically

https://doi.org/10.1017/S0022112005007093 Published online by Cambridge University Press

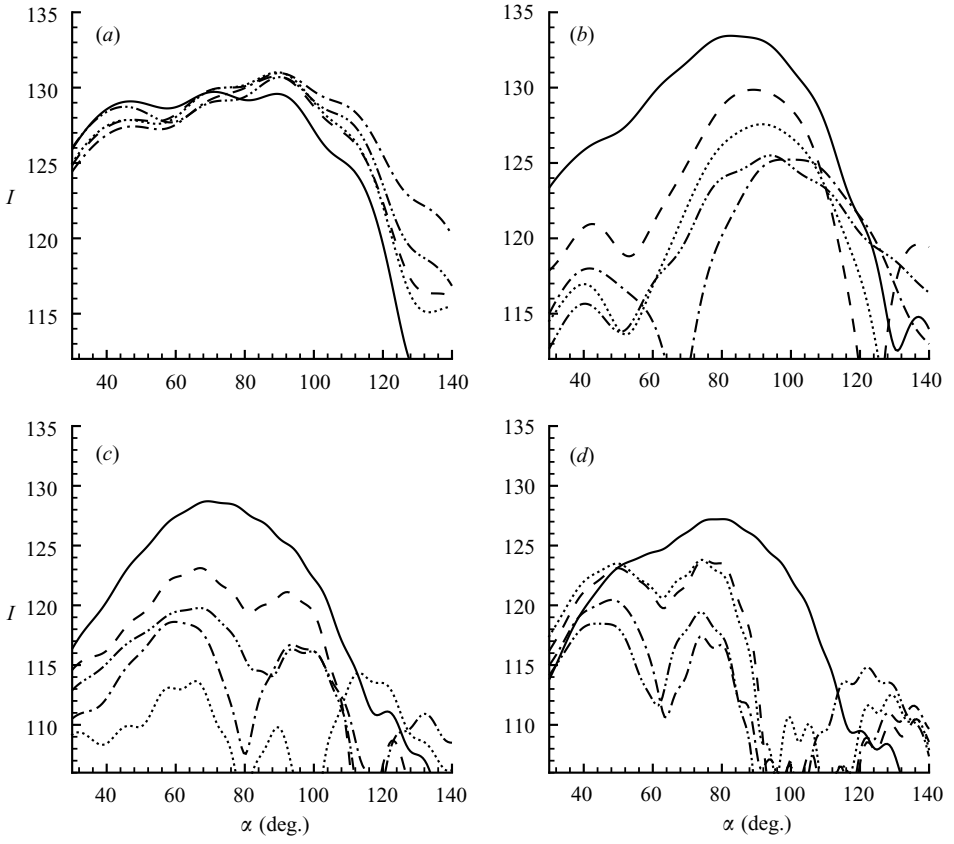


FIGURE 10. Frequency-dependent directivity for frequencies bands (*a*) $0.093 < f/f_0 < 0.133$, (*b*) $0.139 < f/f_0 < 0.179$, (*c*) $0.275 < f/f_0 < 0.315$, and (*d*) $0.343 < f/f_0 < 0.383$: without control (———); and with mass (·····), *x*-direction body force (–··–··), *y*-direction body force (– – – –), and internal energy (–·–·–) control. Angle α is defined in figure 5.

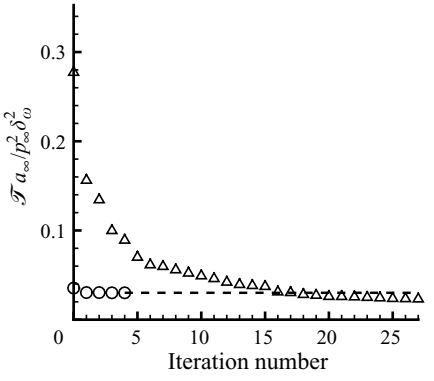


FIGURE 11. The cost reduction by internal energy control in for the randomly (△) and harmonically (○) excited mixing layers.

excited mixing layer discussed in § 2.4. In this case, the noise is not reduced significantly by the control (figure 11). More remarkably, its level nearly matches the noise control limit observed in the randomly excited case. Increasing the amplitude of the harmonic

https://doi.org/10.1017/S0022112005007093 Published online by Cambridge University Press

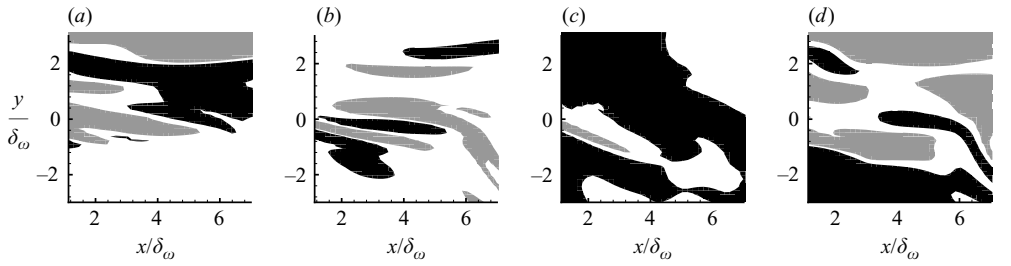


FIGURE 12. The optimized control ϕ at time $100\delta_\omega/a_\infty$: (*a*) mass control; (*b*) x-direction body-force control; (*c*) y-direction body-force control; and (*d*) internal-energy control. Black indicates $\phi > 0.001$, and grey indicates $\phi < -0.001$ in (*a–c*). These limits are ± 0.01 in (*d*).

excitation increases the sound level somewhat but does not increase the effectiveness of our control scheme. By the same reasoning that ordering reduces sound, taking $\alpha^{(i)} = 0$ in (2.5) should also lead to a quieter flow. Indeed, the initial $\mathscr{J}$ in this case falls halfway between the random $\alpha^{(i)}$ case and the harmonically excited case. These observations suggests that the harmonically excited flow is pathologically quiet and that it might, in some sense, be near some lower bound on the noise from this type of unsteady free shear flow, though this is beyond the capabilities of our formulation to prove. Further discussion of these similarities is in § 4.6.3.

4.4. *The optimized control*

Figure 12 shows snapshots of the ϕ in $\mathscr{C}$ for various controls at the same time. The apparent structures we see in ϕ can be shown with space–time correlations to advect at the flow's convection speed, though the integral length scale of the control is shorter than the flow. It is also noteworthy that the internal-energy control has a somewhat longer streamwise correlation length scale than the other controls (Wei 2004). If a price term is added to the cost functional, as discussed in § 3.6, the streamwise correlation of the control is seen to increase somewhat (Wei 2004), which suggests that the more important components of the control are more downstream persistent.

The power needed by the controls is remarkably small. To show this, a relative power function $\eta(t)$ can be defined as a ratio of the control's power to the turbulence kinetic energy flux through a vertical line $\mathscr{L}$ at the downstream edge of $\mathscr{C}$ ($x/\delta_\omega = 7$, $-80 < y/\delta_\omega < 80$). The instantaneous flux is

$$\tilde{F} = \int_{\mathscr{L}} E_k(x_0, y, t)u(x_0, y, t)\,\mathrm{d}y, \tag{4.2}$$

with

$$E_k = \tfrac{1}{2}\rho[(u-\bar{u})^2 + (v-\bar{v})^2], \tag{4.3}$$

so relative the power η for the different cases is defined as

$$\eta_\rho(t) = \frac{1}{\tilde{F}} \int_{\mathscr{C}} \phi_\rho(x, y, t)T_0/\gamma\,\mathrm{d}\boldsymbol{x}, \tag{4.4}$$

$$\eta_u(t) = \frac{1}{\tilde{F}} \int_{\mathscr{C}} \phi_u(x, y, t)u(x, y, t)\,\mathrm{d}\boldsymbol{x}, \tag{4.5}$$

$$\eta_v(t) = \frac{1}{\tilde{F}} \int_{\mathscr{C}} \phi_v(x, y, t)v(x, y, t)\,\mathrm{d}\boldsymbol{x}, \tag{4.6}$$

$$\eta_e(t) = \frac{1}{\tilde{F}} \int_{\mathscr{C}} \phi_e(x, y, t)\,\mathrm{d}\boldsymbol{x}, \tag{4.7}$$

https://doi.org/10.1017/S0022112005007093 Published online by Cambridge University Press

	$\lvert\eta_\rho\rvert$	$\lvert\eta_u\rvert$	$\lvert\eta_v\rvert$	$\lvert\eta_e\rvert$
Maximum	2.25×10^{-2}	5.13×10^{-3}	1.90×10^{-4}	2.27×10^{-1}
Average	1.94×10^{-3}	4.39×10^{-4}	1.87×10^{-5}	2.75×10^{-2}

TABLE 2. The maximum and average power needed by controls in terms of relative power ratio function $|\eta|$.

where the subscripts on η and ϕ refer to mass source (ρ), x-direction body force (u), y-direction body force (v), and internal energy source (e) controls. The maximum and average values of $|\eta|$ are listed in table 2 for each control. We see that the peak η is 0.23, required by an optimized internal-energy control, with corresponding average 0.028. From the viewpoint of required power, the y-direction body-force control is the most efficient, with an average $|\eta_v| = 1.87\times10^{-5}$ and peak $|\eta_v| = 1.90\times10^{-4}$. Defining η based on the mean $\tilde{F}$ yields the same conclusions.

4.5. *Control dimensionality*

The 10^7 control parameters optimized are expected to be far more than is needed to represent an effective control. We can estimate the necessary dimensionality of the control by expanding it in empirical eigenfunctions. From a practical standpoint, the fewer modes needed and the more simple their form, the more likely are effective active controls to be implementable. To obtain appropriate empirical eigenfunctions, we used the proper orthogonal decomposition (Berkooz, Holmes & Lumley 1993), also called the Karhunen–Loève decomposition. Specifically, the method of snapshots (Sirovich 1987) was employed to provide a decomposition of the form

$$\phi(\boldsymbol{x},t) = \sum_{i=1}^{N} a_i(t)\psi_i(\boldsymbol{x}), \tag{4.8}$$

where $\int \psi_i\psi_j \,\mathrm{d}\boldsymbol{x} = \delta_{ij}$ and sums of the form $\sum_{i=1}^{M} a_i(t)\psi_i(\boldsymbol{x})$ for $M < N$ are optimal in the sense of representing the $\overline{\int \phi^2 \,\mathrm{d}\boldsymbol{x}}$ energy. Figure 13 shows the eigenfunction mode energies of the optimized controls. Typically, 50 % of the total control energy is in the first 10 modes, and 75 % is in the first 20. Perfect pairing of the lower modes is seen for the x-direction body-force control, which we shall see in § 4.6 also appears to control the flow somewhat differently than the other controls.

Since these eigenfunctions merely provide a spectral representation of the data, with no direct link to control effectiveness, we must verify that a small number of these modes can indeed be successful. Controls ϕ^M reconstructed with only the M lowest-order modes were thus applied to the original flow. As shown in figure 14, the y-direction body-force control reconstructed with the first mode only, which captures 23 % of the overall $\overline{\int \phi^2 \,\mathrm{d}\boldsymbol{x}}$ energy, reduces the cost $\mathscr{J}$ by 38 % (2.1 dB). With the second mode also included, the y-direction body-force control reduces the cost $\mathscr{J}$ by about 44 % (2.5 dB). This cost reduction is better as more modes are included. When 40 modes are included to rebuild the y-direction body-force control, the cost is reduced by 64 % (4.4 dB), which is close to its full-mode limit 69 % (5.1 dB). The noise reduction by internal-energy source control rebuilt with 40 modes is 82 % (7.4 dB), which is also close to its full-mode limit 92 % (11 dB). Similar effectiveness is observed for all other types of control.

Though a small number of modes can be effective, their form is non-trivial. Figure 15 shows the first four empirical eigenfunction modes for the y-direction

https://doi.org/10.1017/S0022112005007093 Published online by Cambridge University Press

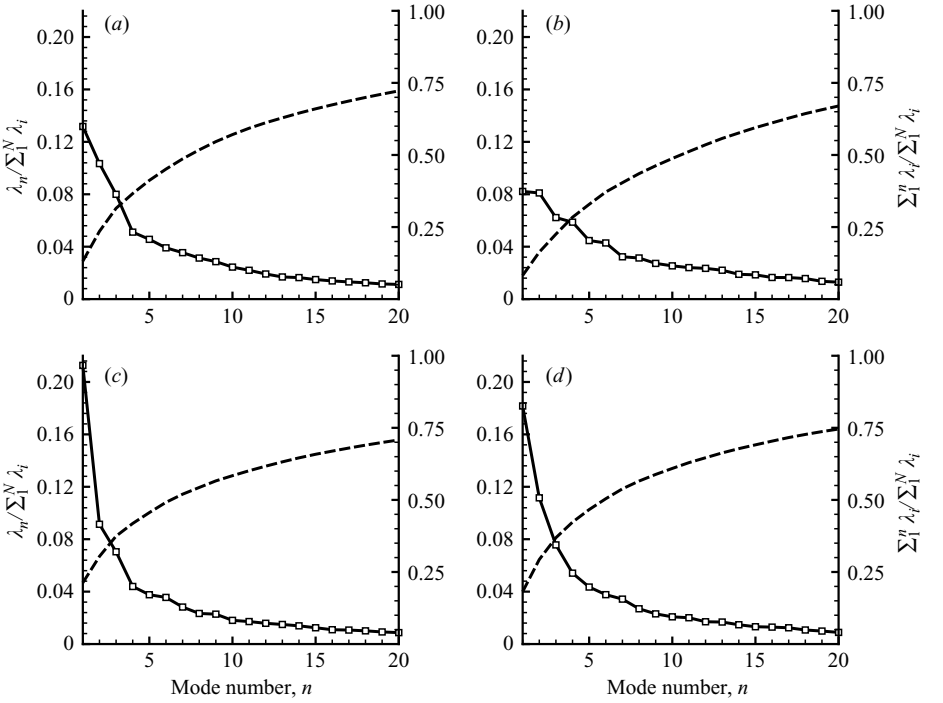


FIGURE 13. Energy of different basis modes λ_i normalized by the sum $\sum_1^N \lambda_i$. ———, Energy of each mode (left axis); – – – –, energy sum of the first n modes (right axis) for: (*a*) mass source, (*b*) x-direction body force, (*c*) y-direction body force, and (*d*) internal-energy source controls.

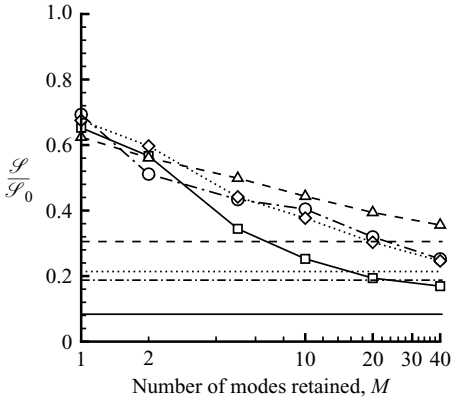


FIGURE 14. Sound reduction by controls rebuilt with the M lowest-order modes (lines with symbols): mass source (·····), x-direction body-force (– – – –), y-direction body-force (–·–·–), and internal-energy (———) controls. Horizontal lines show the full-mode limit. $\mathscr{I}_0$ is the uncontrolled $\mathscr{I}$.

body-force control. The spatial scale appears to be smaller as the mode number increases. The corresponding time coefficients $a_i(t)$ are reported elsewhere (Wei 2004), and have as expected higher frequency content for higher modes. The spatial form of the control is also important. We attempted to control the noise with an *ad hoc*

https://doi.org/10.1017/S0022112005007093 Published online by Cambridge University Press

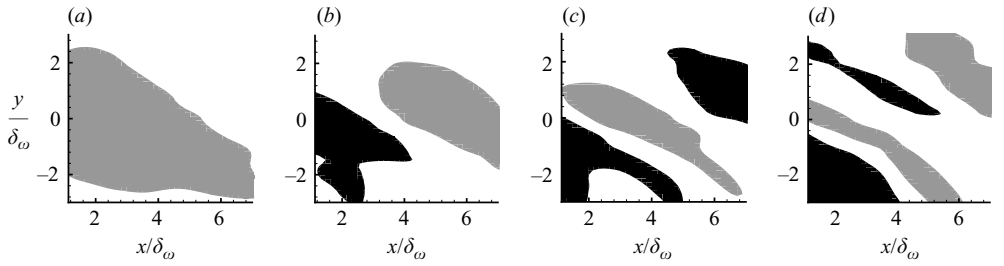


FIGURE 15. Spatial shape of the empirical eigenfunction basis for the control: (*a*) mode 1; (*b*) mode 2; (*c*) mode 3; and (*d*) mode 4. The black shows values lower than −0.15, and the grey shows values higher than 0.15.

pre-specified spatial shape,

$$\phi(\boldsymbol{x}, t) = \hat{\phi}(t) \exp(\sigma_0 |\boldsymbol{x} - \boldsymbol{x}_0|^2), \tag{4.9}$$

with $\boldsymbol{x}_0$ the centre of $\mathscr{C}$ and $\sigma_0 = 0.1$. In this case, the optimized $\hat{\phi}(t)$ for the x-direction body-force control reduces the noise by 44 %, but the other types of control achieved at most a 20 % reduction.

4.6. *Control-induced changes to the flow*

Having the original noisy flow and a perturbed version of it that is significantly quieter provides an opportunity to study the changes that make the flow quiet. The 'before' and 'after' flows are compared in the following subsections.

4.6.1. *Energetic structures*

Several studies of single-frequency or harmonically excited free shear flows (Bridges & Hussain 1992; Ffowcs Williams & Kempton 1978; Laufer & Yen 1983; Colonius *et al.* 1997) suggest some connection between vortex pairing and sound radiation. However, for our randomly excited flow, our control reduces the noise substantially without suppressing pairing or substantially changing the vortex structure at all. In figure 16, visualizations compare the flow before control (figure 16*a*) and after control (figure 16*b–e*), showing little change in the vortical structure of the flow. We heuristically arranged the visualizations of the controlled cases in order of increasing difference from the uncontrolled case. The y-direction body-force control causes almost no noticeable change: figure 16(*b*) is almost indistinguishable from the uncontrolled case in figure 16(*a*). This is also the case that demanded the least control energy. However, the internal-energy control case in figure 16(*c*), which required the most control energy, also appears almost unchanged, but since the control in this case does not directly affect the vorticity, its influence might be expected to be less apparent in this visualization. The mass-control case shown in figure 16(*d*) is noticeably different, but the same pairings seem to occur at approximately the same locations. The x-direction body force in figure 16(*e*) is the only case that appears to have any fundamental difference. These randomly excited flows can be contrasted to the highly organized harmonically excited flow in figure 16(*f*).

To avoid any bias caused by only showing four closely spaced snapshots and to provide a more complete picture of the vortex evolution, in figure 17 we show the entire history of large structures as designated by the pressure fluctuations at $y = 0$. The convergence of low-pressure structures, the black branches in the figure, are an indication of vortex mergings. Again we see slight changes where vorticies merge

https://doi.org/10.1017/S0022112005007093 Published online by Cambridge University Press

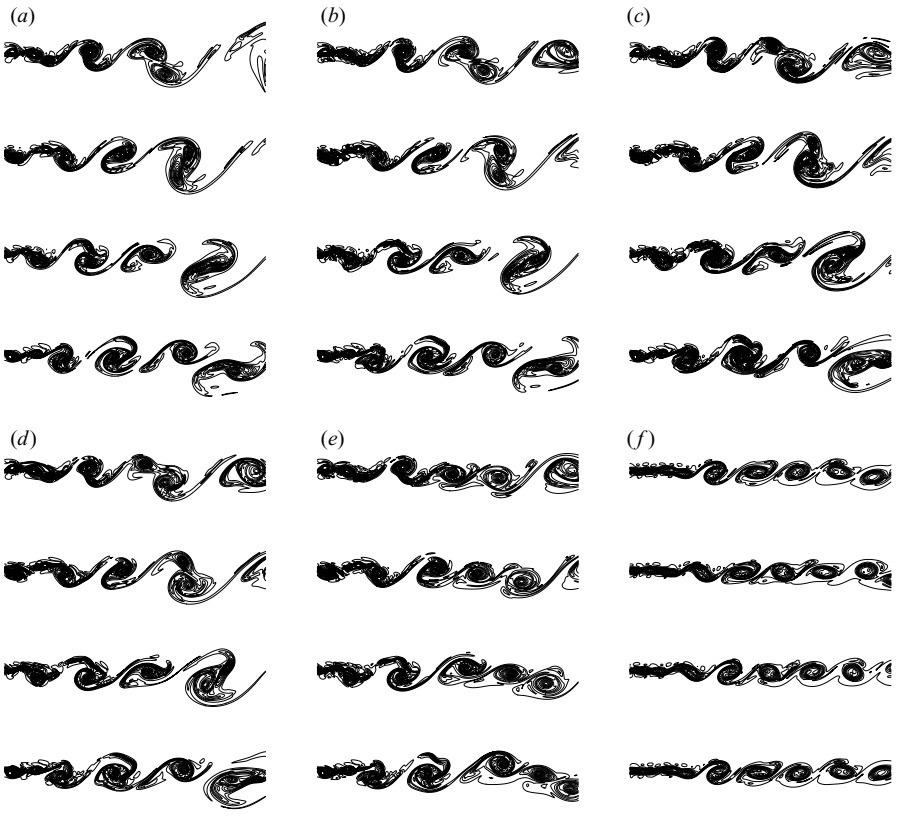


FIGURE 16. Instantaneous vorticity field visualizations at times $ta_\infty/\delta_\omega = 312.5$, 331.0, 351.1, and 371.3, with contour levels from $-0.6\Delta U/\delta_\omega$ to $0.02\Delta U/\delta_\omega$: (*a*) no control; (*b*) *y*-direction body-force control; (*c*) internal-energy source control; (*d*) mass control; (*e*) *x*-direction body-force control; and (*f*) the harmonically excited case, which is indistinguishable before and after control.

and so on, but the changes caused by even the *x*-direction body force in this more complete picture do not indicate any fundamental change, with most (though not all) of the low-pressure mergings occurring near to the locations at which they appear in the uncontrolled case. All these observations bring us to the conclusion that there is no fundamental relation between vortex pairing *per se* and the part of the noise reduced by our controls in the present mixing layers.

4.6.2. *Mean-flow and fluctuation statistics*

Given the qualitative similarity of the flow before and after the control is applied, one should not be surprised that the mean flow and turbulence statistics are also nearly unchanged. Figure 18(*a*) shows that momentum thickness, defined by

$$\delta_m = \int_{y_a}^{y_b} \frac{\rho(u - U_a)(U_b - u)}{\rho_\infty \Delta U^2}\, \mathrm{d}y, \tag{4.10}$$

is nearly linear in x and only slightly changed by any of the controls for all four cases, though they all suppress spreading slightly around $x = 60\delta_\omega$. In (4.10), U_a and U_b are the x-velocity at y_a and y_b and results were, of course, insensitive to the y_a and y_b.

https://doi.org/10.1017/S0022112005007093 Published online by Cambridge University Press

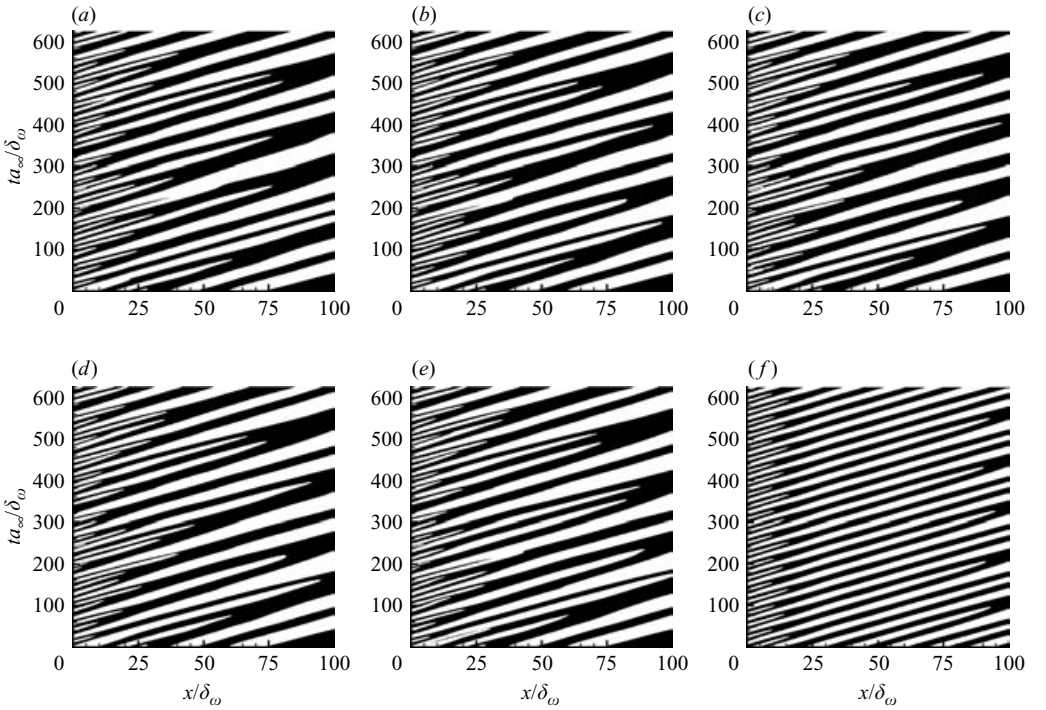


FIGURE 17. Pressure evolution at $y = 0$: (*a*) no control; (*b*) *y*-direction body-force control; (*c*) internal energy source control; (*d*) mass control; (*e*) *x*-direction body-force control; and the (*f*) harmonically excited case. Black is $(p - p_\infty) < 0$; white is $(p - p_\infty) > 0$.

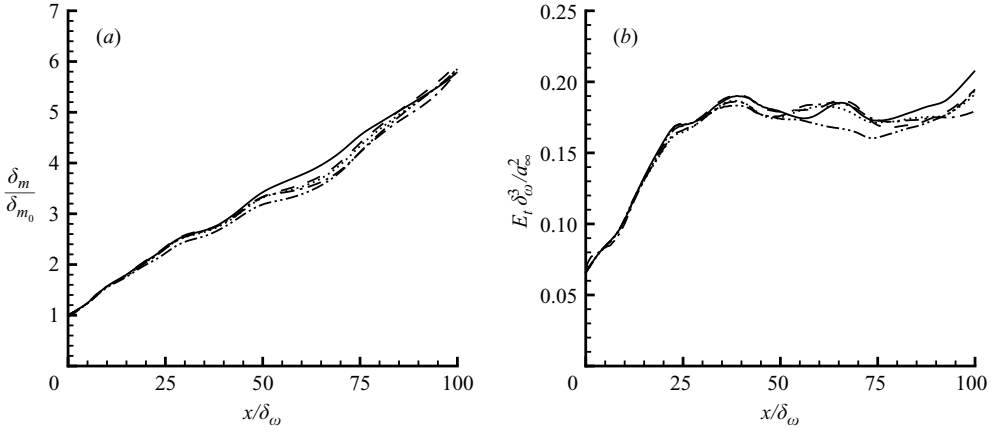


FIGURE 18. (*a*) Momentum thickness (4.10) of the mean flow (normalized by δ_{m_0}, the initial momentum thickness at $x = 0$). (*b*) Fluctuation kinetic energy integrated in the *y*-direction (4.11). Lines in both figures show cases without control (———); and with mass (·····) source control, *x*-direction body force (–··–··), *y*-direction body force (– – – –), and internal-energy source (–·–·–) controls.

https://doi.org/10.1017/S0022112005007093 Published online by Cambridge University Press

Second-order statistics of the flow fluctuations are also nearly unchanged. With E_k defined in (4.3), the y-integrated mean fluctuation kinetic energy normalized by the local mean momentum thickness (4.10),

$$E_t(x) = \frac{\displaystyle\int_{-80\delta_\omega}^{80\delta_\omega} \overline{E_k}\,\mathrm{d}y}{\delta_m(x)}, \tag{4.11}$$

is plotted in figure 18(*b*). This quantity reaches its maximum near $x = 25\delta_\omega$ and remains constant downstream. The control was applied from $x = \delta_\omega$ to $x = 7\delta_\omega$, where the turbulence intensity is about 70 % of its fully developed level, though the mixing layer is already spreading linearly at this point and at the same rate as for large x. Thus, the control was optimized and applied in a region where the unsteady flow fluctuations have amplitudes close to their nonlinearly saturated condition. Moving $\mathscr{C}$ further downstream to where the fluctuations are somewhat more intense and increasing its size in proportion to the local momentum thickness showed similar success. The small effect of the control on the flow is clear in that the turbulence kinetic energy has not been changed much by the controls. The noise control is not by a suppression of the unsteady fluctuations.

4.6.3. *Evolution of the energetic flow structures*

Based on these results, it is clear that subtle aspects of the manner in which the fluctuation energy is arranged in the flow must be responsible for the noise reduction we observe. Assuming for discussion the simplest description of sound source and propagation discussed in § 1, it is potentially subtle aspects of their evolution as they advect downstream that puts energy into components with supersonic phase velocity in x, which can then radiate to the far field in y. The specific interactions that disrupt smooth advection in x are, however, difficult to quantify. Interactions with a short length scale in x, or similarly on a short time scale, will broaden the corresponding Fourier transforms in k and ω and thus potentially increase energy in components that can radiate. However, analysis of direct numerical simulation data suggests that all Fourier modes participate in the interaction (Freund, Bodony & Lele 2002).

Here we seek a means of assessing how smoothly the flow's energy advects downstream. For convecting structures in a quiet streamwise homogeneous flow, we would expect to find that the flow's fluctuations would be representable by Fourier modes with only subsonic (or mostly subsonic) phase velocities. A way for them to be quiet would be for them to advect nearly unchanged, which would give them a form such as $a_1(t)\cos kx + a_2(t)\sin kx$, with $a_1(t)$ and $a_2(t)$ tracing circles in their phase plane. In the present streamwise inhomogeneous case, Fourier transforms are clumsy (e.g. Freund 2001). Though they do provide a definitive partitioning of the energy into radiating and non-radiating components, their physical interpretation is clouded by the fact that individual k–ω modes may extend beyond the length of the physical flow. Therefore, we employ empirical eigenfunctions in the inhomogeneous-flow x-direction to assess the advection of energy. The proper orthogonal decomposition is again used here to provide empirical basis functions as it has been used in numerical and experimental efforts in designating flow structures in jets (Arndt, Long & Glauser 1997; Freund & Colonius 2002; Hileman *et al.* 2004). We define the empirical eigenfunctions by a kinetic energy norm

$$\|\boldsymbol{q}\|^2 = \int_{D_p} (u^2 + v^2)\,\mathrm{d}\boldsymbol{x}, \tag{4.12}$$

https://doi.org/10.1017/S0022112005007093 Published online by Cambridge University Press

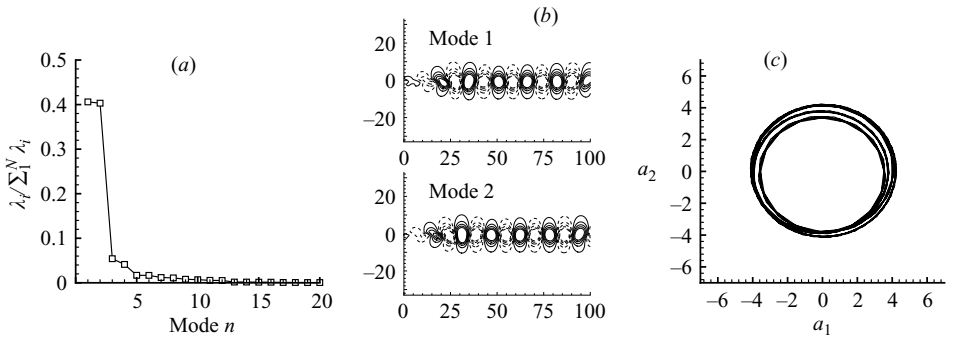


FIGURE 19. The empirical eigenmodes of the harmonically excited mixing layer: (*a*) relative mode energy as in figure 13; (*b*) the ρv component of modes 1 and 2 with solid lines showing positive and dashed showing negative contours; and (*c*) the phase plane of the coefficients of modes 1 and 2.

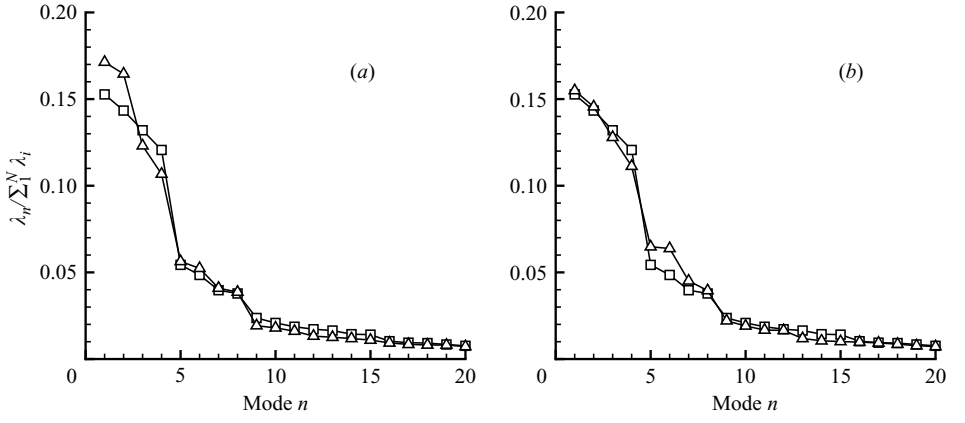


FIGURE 20. Relative energy represented by the lowest-order empirical eigenfunctions before (□) and after (△) control: (*a*) *y*-direction body-force and (*b*) *x*-direction body-force controls.

where D_p is the entire physical domain in our computation, and can then reconstruct the flow by

$$\boldsymbol{q}(\boldsymbol{x}, t) = \sum_{i=1}^{N} a_i(t)\boldsymbol{\psi}_i(\boldsymbol{x}). \tag{4.13}$$

Taking the harmonically excited mixing layer as an example, we see that the kinetic energy of the two most energetic modes is nearly the same (figure 19*a*), the corresponding modes fit together as sines and cosines (figure 19*b*), and their time coefficients trace circular trajectories in their phase plane (figure 19*c*). This is the type of behaviour that we anticipated for this quiet flow. Remarkably, we can observe a switch to this type of underlying behaviour with the application of our control even in the randomly excited flow.

We focus on the *y*-direction body-force control case for discussion, but the results are general. Figure 20(*a*) shows the relative energy represented by each eigenfunction before and after the *y*-direction body-force control is applied. While they are similar before and after, it is noteworthy that mode energy levels become more closely paired

https://doi.org/10.1017/S0022112005007093 Published online by Cambridge University Press

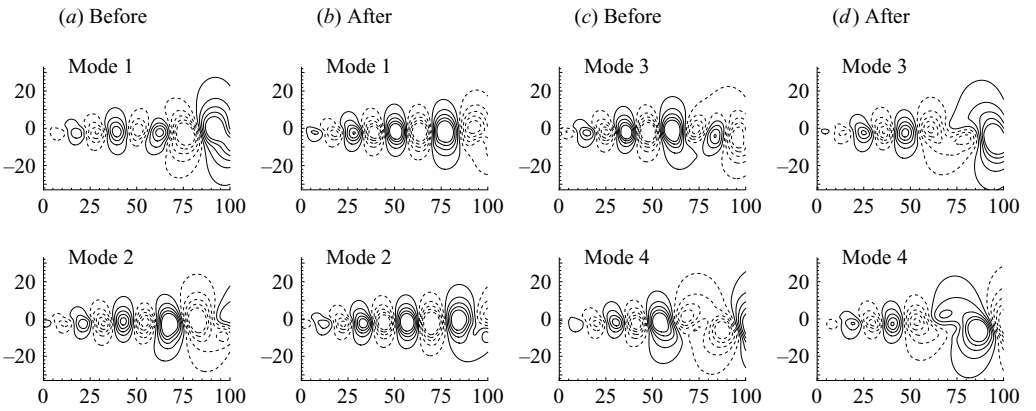


FIGURE 21. The ρv component of the four most energetic empirical eigenfunction modes before and after y-direction body-force control with solid contours showing positive levels $\leqslant 0.03$ and dashed contours showing negative levels $\geqslant -0.03$.

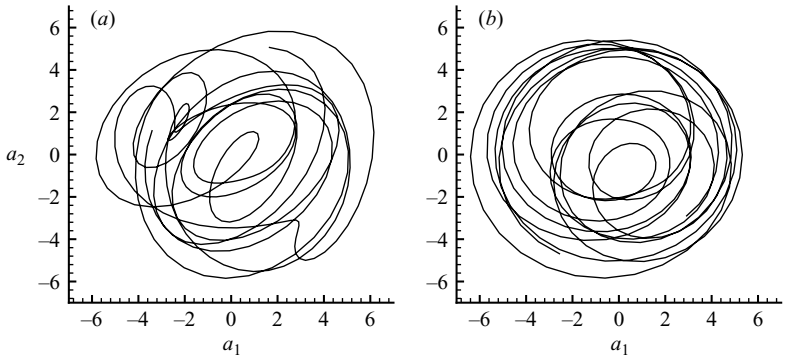


FIGURE 22. Phase map of the coefficients of the first two empirical eigenfunctions (*a*) before and (*b*) after y-direction body-force control.

up to mode eight. The eigenfunctions also pair up. Figure 21 shows the y-momentum components of the vector-valued eigenmodes. After control, they become close out-of-phase pairs, like sines and cosines. Further, and perhaps more importantly, their time-dependent coefficients now give their net behaviour a smoother downstream travelling character. Figure 22 shows the coefficients $a_1(t)$ and $a_2(t)$ of the first two modes before and after the control is applied. The x-momentum components of the eigenmodes show similar behaviour.

The cases using mass control and internal-energy control show very similar behaviour to that discussed above for the y-direction body-force control. However, for the x-direction body-force control, the energy of each mode is paired up differently (see figure 20*b*). It seems to couple the fifth and sixth eigenmodes of the flow. For the y-direction momentum components of the modes (see figure 23*a*, *b*), a coupling into sine- and cosine-like modes occurs for modes 5 and 6. Correspondingly, the phase picture of the coefficients $a_5(t)$ and $a_6(t)$ also shows more circular motion compared with the original flow (figure 23*c*, *d*). We saw in figure 10 that this control is more successful at higher frequencies than the y-body-force control.

https://doi.org/10.1017/S0022112005007093 Published online by Cambridge University Press

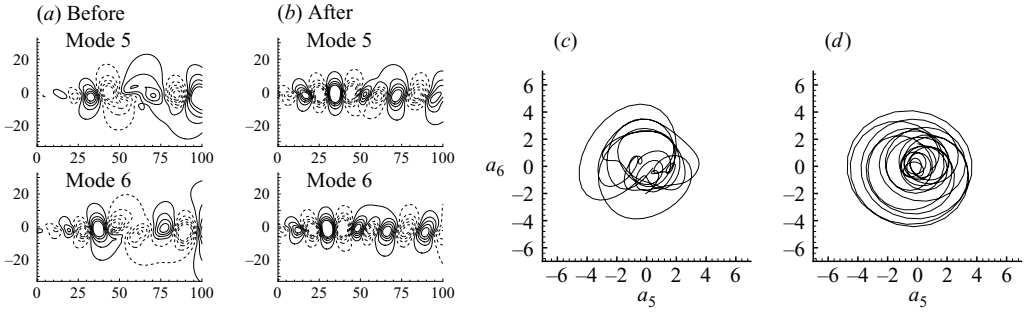


FIGURE 23. (a, b) The ρv component of modes 5 and 6 before and after x-direction body-force control with solid contours showing positive levels $\leqslant 0.03$ and dashed contours showing negative levels $\geqslant -0.03$. Also shown are the phase maps of the coefficients of the these modes (c) before and (d) after x-direction body-force control.

5. Discussion and conclusions

In summary, the adjoint-based optimal control framework that we formulated and implemented was able to circumvent the complexity of the flow's interactions leading to noise generation and significantly reduce it directly. It 'chose' to do this by subtly changing the evolution of the existing turbulence structures in the flow. Only slight changes in the locations of pairing and other identifiable events were noted and the turbulence statistics were nearly unchanged by the control. Since essentially the same vortex pairings were observed before and after the application of the control, we conclude that it is not pairings *per se* or any other clearly identifiable near-field flow mechanics that are responsible for making a considerable fraction of the total noise.

The clearest picture of the changes to the flow came from decomposing it into empirical eigenfunctions, which show that the controlled turbulence structures advect more uniformly downstream. The eigenfunctions of the controlled flow are in sin–cos like pairs, with coefficients that trace relatively circular trajectories in their respective phase planes. This interpretation was reinforced by results for a harmonically (as opposed to randomly) excited mixing layer. In this case the control was ineffective, but the flow was already acoustically inefficient, radiating comparably to the controlled randomly excited cases. The empirical eigenfunctions also shared key features with the randomly excited but controlled flow. They were, as expected, in distinct sin–cos pairs whose coefficients traced near perfect circles in their corresponding phase plane.

It has long been understood that the largest turbulent flow structures in inflectional free shear flow bear considerable resemblance to the linear instability modes supported by the same flow. This is especially true in two-dimensional flow, which lacks the vortex stretching mechanism for removing energy from these structures via the turbulence energy cascade. Such similarity has inspired several efforts to model aspects of free-shear-flow noise using wave-packet models for the noise sources. These have included attempts based on both actual linear instability modes (Huerre & Crighton 1983; Mankbadi & Liu 1984) and relatively *ad hoc* wave packets, which match the qualitative character of growing then decaying instability modes (Crighton & Huerre 1990; Ffowcs Williams & Kempton 1978). Collectively, these have met with some success, often predicting aspects (e.g. functional forms) of observed experimental results, but typically are not complete, predicting for example erroneous angles of silence (Huerre & Crighton 1983; Mankbadi & Liu 1984). A factor contributing to this difficulty is the remarkable sensitivity of sources of this form to perturbations, which presumably occur due to nonlinearity in any nonlinearly active free shear flow,

https://doi.org/10.1017/S0022112005007093 Published online by Cambridge University Press

making it louder. One can speculate that a free shear flow, at least a relatively simple two-dimensional one, is in some sense near an acoustically less efficient unperturbed wave-packet state. Based upon the results presented in § 4.6.3, such an acoustically inefficient state has been found by our control. Supporting this view, the angles of silence observed for narrow frequency bands (figure 10) are similar to those predicted by some wave-packet-based models. Three-dimensional turbulent flows are also known to have an underlying instability-wave-like character, but it remains to be seen if they can be perturbed into a quieter state as easily as the present two-dimensional flow.

Though we have optimized the control, no conclusions can be made about whether or not this control is truly optimal and does not just represent a local minimum. It is possible that a quieter flow might be achieved by starting from a different ϕ point. A laminar flow would be an obvious target state, but what specific control could achieve this in a free shear flow is unclear when the slightest disturbance will once again seed instability growth and eventual nonlinear development in the flow. In contrast, the optimized control we found appears to be a stable local minimum. Regardless, laminarization is probably not a possibility for the selected $\mathscr{C}$ because it does not extend entirely across the thickness of the mixing layers.

From a practical perspective, an attractive feature of the identified control is that it is a relatively minor perturbation to the flow that does not change the fundamental hydrodynamics, though it remains unclear how one might find such a controller in practice. Unfortunately, the control itself was also complex, defying any clear interpretation. Based on space–time correlations, it was seen to advect in its region of support at the same speed as the local flow structures. A decomposition into empirical eigenfunctions showed that controls reconstructed with only one or two modes, which capture only 20 % to 30 % of the energy, achieved 40 % to 50 % sound reduction. Optimizing only the time coefficient of a Gaussian-pulse-shaped actuation reduced the noise up to 44 %, but was only this successful for the x-direction body-force control.

The authors thank Professor Clancy Rowley for helpful discussions about the adjoint formulation and empirical eigenfunction analysis. We also gratefully acknowledge the financial support from AFOSR and the computer resources provided by NPACI and NCSA.

Appendix A. Compressible viscous flow equations

The compressible viscous flow equations were written in an operator form as

$$\mathscr{N}(\boldsymbol{q}) = [n_1(\boldsymbol{q})\ \ n_2(\boldsymbol{q})\ \ n_3(\boldsymbol{q})\ \ n_4(\boldsymbol{q})]^T = 0, \tag{A 1}$$

with

$$\left.\begin{aligned}
n_1(\boldsymbol{q}) &= \frac{\partial \rho}{\partial t} + \frac{\partial \rho u}{\partial x} + \frac{\partial \rho v}{\partial y},\\
n_2(\boldsymbol{q}) &= \frac{\partial \rho u}{\partial t} + \frac{\partial \rho u u}{\partial x} + \frac{\partial \rho u v}{\partial y} + \frac{\partial p}{\partial x} - \frac{1}{Re}\left(\frac{4}{3}\frac{\partial^2 u}{\partial x^2} + \frac{\partial^2 u}{\partial y^2} + \frac{1}{3}\frac{\partial^2 v}{\partial x \partial y}\right),\\
n_3(\boldsymbol{q}) &= \frac{\partial \rho v}{\partial t} + \frac{\partial \rho u v}{\partial x} + \frac{\partial \rho v v}{\partial y} + \frac{\partial p}{\partial y} - \frac{1}{Re}\left(\frac{4}{3}\frac{\partial^2 v}{\partial y^2} + \frac{\partial^2 v}{\partial x^2} + \frac{1}{3}\frac{\partial^2 u}{\partial x \partial y}\right),\\
n_4(\boldsymbol{q}) &= \frac{\partial e}{\partial t} + \frac{\partial}{\partial x}[u(e+p)] + \frac{\partial}{\partial y}[v(e+p)] - \frac{\gamma}{RePr(\gamma-1)}\left[\frac{\partial^2}{\partial x^2}\left(\frac{p}{\rho}\right) + \frac{\partial^2}{\partial y^2}\left(\frac{p}{\rho}\right)\right]\\
&\quad - \frac{1}{Re}\left[\frac{\partial}{\partial x}(\tau_{xx}u + \tau_{xy}v) + \frac{\partial}{\partial y}(\tau_{yx}u + \tau_{yy}v)\right],
\end{aligned}\right\} \tag{A 2}$$

https://doi.org/10.1017/S0022112005007093 Published online by Cambridge University Press

where stresses τ_{ij} are for a Newtonian fluid with zero bulk viscosity, and the total energy e for our normalization is

$$e = \frac{p}{\gamma - 1} + \frac{1}{2}\rho(u^2 + v^2), \tag{A 3}$$

including both internal and kinetic energy. Here, all variables were non-dimensionalized with ρ_∞, a_∞, δ_ω, and c_p, which gives a dimensionless gas constant $R = (\gamma - 1)/\gamma$, where γ is the ratio of the specific heats, and $Re = \rho_\infty a_\infty \delta_\omega / \mu$.

Appendix B. Adjoint equations

Following the systematic procedure in § 3.3, the adjoint of the linearized perturbed compressible viscous flow equations is

$$\mathscr{N}^*(\boldsymbol{q})\boldsymbol{q}^* = \left(\boldsymbol{C}^*\frac{\partial}{\partial t} + \boldsymbol{A}^*\frac{\partial}{\partial x} + \boldsymbol{B}^*\frac{\partial}{\partial y} + \boldsymbol{D}^*\right)\boldsymbol{q}^*, \tag{B 1}$$

where

$$\boldsymbol{A}^* = \begin{bmatrix} u & u^2 & uv & \frac{1}{2}u(u^2+v^2) \\ \rho & 2\rho u & \rho v & \dfrac{\gamma p}{\gamma-1} + \frac{1}{2}\rho(3u^2+v^2) + \dfrac{5}{3Re}\dfrac{\partial v}{\partial y} \\ 0 & 0 & \rho u & \rho uv - \dfrac{5}{3Re}\dfrac{\partial u}{\partial y} \\ 0 & \gamma - 1 & 0 & \gamma u \end{bmatrix}, \tag{B 2}$$

$$\boldsymbol{B}^* = \begin{bmatrix} v & uv & v^2 & \frac{1}{2}v(u^2+v^2) \\ 0 & \rho v & 0 & \rho uv - \dfrac{5}{3Re}\dfrac{\partial v}{\partial x} \\ \rho & \rho u & 2\rho v & \dfrac{\gamma p}{\gamma-1} + \frac{1}{2}\rho(u^2+3v^2) + \dfrac{5}{3Re}\dfrac{\partial u}{\partial x} \\ 0 & 0 & \gamma - 1 & \gamma v \end{bmatrix}, \tag{B 3}$$

$$\boldsymbol{C}^* = \begin{bmatrix} 1 & u & v & \frac{1}{2}(u^2+v^2) \\ 0 & \rho & 0 & \rho u \\ 0 & 0 & \rho & \rho v \\ 0 & 0 & 0 & 1 \end{bmatrix}, \tag{B 4}$$

and

$$\boldsymbol{D}^* = \frac{1}{Re}\begin{bmatrix} 0 & 0 & 0 & -\dfrac{\gamma\, p}{Pr\,(\gamma-1)\,\rho^2}\left(\dfrac{\partial^2}{\partial x^2} + \dfrac{\partial^2}{\partial y^2}\right) \\ 0 & \dfrac{4}{3}\dfrac{\partial^2}{\partial x^2} + \dfrac{\partial^2}{\partial y^2} & \dfrac{1}{3}\dfrac{\partial^2}{\partial x \partial y} & \dfrac{4u}{3}\dfrac{\partial^2}{\partial x^2} + u\dfrac{\partial^2}{\partial y^2} + \dfrac{v}{3}\dfrac{\partial^2}{\partial x \partial y} \\ 0 & \dfrac{1}{3}\dfrac{\partial^2}{\partial x \partial y} & \dfrac{4}{3}\dfrac{\partial^2}{\partial y^2} + \dfrac{\partial^2}{\partial x^2} & \dfrac{4v}{3}\dfrac{\partial^2}{\partial y^2} + v\dfrac{\partial^2}{\partial x^2} + \dfrac{u}{3}\dfrac{\partial^2}{\partial x \partial y} \\ 0 & 0 & 0 & \dfrac{\gamma}{Pr\,\rho}\left(\dfrac{\partial^2}{\partial x^2} + \dfrac{\partial^2}{\partial y^2}\right) \end{bmatrix}. \tag{B 5}$$

These matrices all depend on the flow solutions, ρ, u, v, and p. In the numerical solution, $\boldsymbol{C}^*$ was inverted every Runge–Kutta sub-step. The adjoint has

https://doi.org/10.1017/S0022112005007093 Published online by Cambridge University Press

a similar characteristics structure as the flow equations, which permits a one-dimensional characteristic boundary condition to be developed in a similar fashion (Wei 2004).

REFERENCES

Arndt, R. E. A., Long, D. F. & Glauser, M. N. 1997 The proper orthogonal decomposition of pressure fluctuations surrounding a turbulent jet. *J. Fluid Mech.* **340**, 1–33.

Berkooz, G., Holmes, P. & Lumley, J. L. 1993 The proper orthogonal decomposition in the analysis of turbulent flows. *Annu. Rev. Fluid Mech.* **25**, 539–575.

Bewley, T. R., Moin, P. & Temam, R. 2001 DNS-based predictive control of turbulence: an optimal benchmark for feedback algorithms. *J. Fluid Mech.* **447**, 179–225.

Bridges, J. & Hussain, F. 1992 Direct evaluation of aeroacoustic theory in a jet. *J. Fluid Mech.* **240**, 469–501.

Colonius, T., Lele, S. K. & Moin, P. 1997 Sound generation in a mixing layer. *J. Fluid Mech.* **330**, 375–409.

Crighton, D. G. 1975 Basic principles of aerodynamic noise generation. *Prog. Aerospace Sci.* **16**, 31–96.

Crighton, D. G. & Huerre, P. 1990 Shear-layer pressure fluctuations and superdirective acoustic sources. *J. Fluid Mech.* **220**, 255–368.

Ffowcs Williams, J. E. 1963 The noise from turbulence convected at high speed. *Phil. Trans. R. Lond. Soc.* A **255**, 469–503.

Ffowcs Williams, J. E. & Kempton, A. J. 1978 The noise from the large-scale structure of a jet. *J. Fluid Mech.* **84**, 673–694.

Freund, J. B. 1997 A proposed inflow/outflow boundary condition for direct computation of aerodynamic sound. *AIAA J.* **35**, 740–742.

Freund, J. B. 2001 Noise sources in a low-Reynolds-number turbulent jet at Mach 0.9. *J. Fluid Mech.* **438**, 277–305.

Freund, J. B., Bodony, D. J. & Lele, S. K. 2002 Turbulence interactions leading to far-field jet noise. *Center for Turbulence Research, Proceedings of the Summer Program 2002*, pp. 15–25. Stanford University.

Freund, J. B. & Colonius, T. 2002 POD analysis of sound generation by a turbulent jet. A *AIAA Paper* 2002-0072.

Goldstein, M. E. 2003 A generalized acoustic analogy. *J. Fluid Mech.* **488**, 315–333.

Hileman, J., Caraballo, E., Thurow, B. & Samimy, M. 2004 Difference in dynamics of an idealy expanded Mach 1.3 jet during noise generation and relative quiet periods. *AIAA Paper* 2004-3015.

Huerre, P. & Crighton, D. G. 1983 Sound generation by instability waves in a low Mach number jet. *AIAA Paper* 83-0661.

Laufer, J. & Yen, T.-C. 1983 Noise generation by a low-Mach-number jet. *J. Fluid Mech.* **134**, 1–31.

Lele, S. K. 1992 Compact finite difference schemes with spectral-like resolution. *J. Comput. Phys.* **103**, 16–42.

Lighthill, M. J. 1952 On sound generated aerodynamically: I. General theory. *Proc. Royal Soc. Lond.* A **211**, 564–587.

Mankbadi, R. & Liu, J. T. C. 1984 Sound generated aerodynamically revisited: large-scale structures in a turbulent jet as a source of sound. *Phil. Trans. R. Soc. Lond.* A **311**, 183–217.

Mitchell, B. E., Lele, S. K. & Moin, P. 1999 Direct computation of the sound generated by vortex pairing in an axisymmetric jet. *J. Fluid Mech.* **383**, 113–142.

Monkewitz, P. A. & Huerre, P. 1982 Influence of the velocity ratio on the spatial instabilty of mixing layers. *Phys. Fluids* **25**, 1137–1143.

Press, W. H., Flannery, B. P., Teukolsky, S. A. & Vetterling, W. T. 1986 *Numerical Recipes.* Cambridge University Press.

Sandham, N. & Reynolds, W. 1991 Three-dimensional simulations of large eddies in the compressible mixing layer. *J. Fluid Mech.* **224**, 133–158.

https://doi.org/10.1017/S0022112005007093 Published online by Cambridge University Press

Sirovich, L. 1987 Chaotic dynamics of coherent structures. Parts I–III. *Q. Appl. Maths* **XLV**, 561–582.

Tam, C. K. W. & Webb, J. C. 1993 Dispersion-relation-preserving finite difference schemes for computational acoustics. *J. Comput. Phys.* **107**, 262–281.

Vainberg, M. M. 1964 *Variational Methods for the Study of Nonlinear Operators*. San Francisco: Holden-Day.

Wei, M. 2004 Jet noise control by adjoint-based optimization. PhD thesis, Department of Theoretical and Applied Mechanics, University of Illinois at Urbana-Champaign, Urbana, Illinois.

https://doi.org/10.1017/S0022112005007093 Published online by Cambridge University Press